

# End-to-end Adaptive Dynamic Subsampling and Reconstruction for Cardiac MRI

George Yiasemis<sup>1,2</sup>, Jan-Jakob Sonke<sup>1,2</sup>, Jonas Teuwen<sup>1,2,3</sup>  
 {g.yiasemis, j.sonke, j.teuwen}@nki.nl

<sup>1</sup> Netherlands Cancer Institute, Amsterdam, Netherlands

<sup>2</sup> University of Amsterdam, Amsterdam, Netherlands

<sup>3</sup> Radboud University Medical Center, Nijmegen, Netherlands

## Abstract.

**Background:** Accelerating dynamic MRI is vital for advancing clinical applications and improving patient comfort. Commonly, deep learning (DL) methods for accelerated dynamic MRI reconstruction typically rely on uniformly applying non-adaptive predetermined or random subsampling patterns across all temporal frames of the dynamic acquisition. This approach fails to exploit temporal correlations or optimize subsampling on a case-by-case basis.

**Purpose:** To develop an end-to-end approach for adaptive dynamic MRI subsampling and reconstruction, capable of generating customized sampling patterns maximizing at the same time reconstruction quality.

**Methods:** We introduce the End-to-end Adaptive Dynamic Sampling and Reconstruction (E2E-ADS-Recon) for MRI framework, which integrates an adaptive dynamic sampler (ADS) that adapts the acquisition trajectory to each case for a given acceleration factor with a state-of-the-art dynamic reconstruction network, vSHARP, for reconstructing the adaptively sampled data into a dynamic image. The ADS can produce either frame-specific patterns or unified patterns applied to all temporal frames. E2E-ADS-Recon is evaluated under both frame-specific and unified 1D or 2D sampling settings, using dynamic cine cardiac MRI data and compared with vSHARP models employing standard subsampling trajectories, as well as pipelines where ADS was replaced by parameterized samplers optimized for dataset-specific schemes.

**Results:** E2E-ADS-Recon exhibited superior reconstruction quality, especially at high accelerations, in terms of standard quantitative metrics (SSIM, pSNR, NMSE).

**Conclusion:** The proposed framework improves reconstruction quality, highlighting the importance of case-specific subsampling optimization in dynamic MRI applications.

**Keywords:** Adaptive MRI Sampling · Dynamic MRI · Accelerated MRI

## 1 Introduction

Magnetic Resonance Imaging (MRI) represents an important clinical imaging modality. However, its inherently slow acquisition and susceptibility to motion—stemming from respiratory, bowel, or cardiac movements—pose significant

challenges, especially for dynamic imaging. These factors hinder the collection of fully-sampled dynamic frequency domain measurements, known as  $k$ -space, leading to degraded image quality. Consequently, patients are often required to perform actions like voluntary breath-holding to minimize motion effects. To address these issues, accelerated dynamic acquisition techniques, which involve subsampling of the  $k$ -space below the Nyquist ratio [23], have been employed.

Recent advancements have seen Deep Learning (DL)-based MRI reconstruction methods significantly outperforming traditional approaches such as Compressed Sensing (CS) [15,6]. These DL methods excel in reconstructing MRI images from highly-accelerated measurements [8,37]. Despite the predominant focus on static MRI reconstruction due to limited reference dynamic acquisitions, recent developments have extended to dynamic MRI reconstruction [14,21,34,40,41].

Nonetheless, a critical limitation persists in DL-based dynamic MRI reconstruction. Current methodologies typically rely on predetermined, often arbitrary, subsampling patterns, uniformly applied across all temporal frames. This approach overlooks the benefits of exploiting temporal correlations present in adjacent frames and the potential superiority of DL-based learned adaptive sampling schemes, which constitutes our primary motivation.

Previous studies have demonstrated the feasibility of learning optimized on training data sampling schemes at specific acceleration factors, trained jointly with a reconstruction network in single [1] or multi-coil [42] settings. In the context of adaptive sampling, various DL-based sampling approaches have been proposed in both single [19,29,39,2] and multi-coil [3,7] scenarios.

While, these methods have primarily been applied to static data, a recent study [24] proposes a method to address dynamic acquisitions by learning a single non-adaptive optimized dynamic non-Cartesian trajectory, trained alongside a reconstruction model. To the best of our knowledge, this approach is unique in its focus on learning dynamic sampling from training data. Yet, it does not explore *adaptiveness*, nor does it support varying acceleration rates, leaving the field of adaptive dynamic Cartesian subsampling unexplored. Our work aims to fill this gap. Our contributions can be summarized as follows:

- We introduce E2E-ADS-Recon, a novel end-to-end *learned adaptive dynamic subsampling and reconstruction method* for dynamic, multi-coil, Cartesian MRI data. This method integrates an adaptive dynamic sampling model with a sensitivity map prediction module and the DL-based state-of-the-art vSHARP dynamic MRI reconstruction method [36], all trained *end-to-end*. Our approach is designed for simultaneous training across *varying acceleration factors*.
- We propose two dynamic sampling methodologies: one that learns distinct adaptive trajectories for each frame (*frame-specific*) and another that learns a uniform adaptive trajectory for all frames (*unified*), with both methods applied to 1D (line) and 2D (point) sampling.
- We evaluate our pipeline on a multi-coil, dynamic cardiac MRI dataset [31]. Our evaluations include comparisons with pipelines where dynamic subsampling schemes are dataset-optimized or use fixed or random schemes.

## 2 Materials and Methods

### 2.1 Accelerated Dynamic MRI Acquisition and Reconstruction

Given a sequence of fully-sampled dynamic multi-coil  $k$ -space data  $\mathbf{y} \in \mathbb{C}^{n \times n_c \times n_f}$ , the underlying dynamic image  $\mathbf{x}^* \in \mathbb{C}^{n \times n_f}$ , can be obtained by applying the inverse Fast Fourier transform  $\mathcal{F}^{-1}$ :  $\mathbf{x}^* = \mathcal{F}^{-1}(\mathbf{y})$ , where  $n = n_1 \times n_2$ ,  $n_c$ , and  $n_f$  represent the spatial dimensions, the number of coils, and the number of frames (time-steps) of the dynamic acquisition, respectively. To accelerate the acquisition, the  $k$ -space is subsampled. The acquired subsampled dynamic multi-coil  $k$ -space  $\tilde{\mathbf{y}} \in \mathbb{C}^{n \times n_c \times n_f}$  can be defined by the forward problem:

$$\tilde{\mathbf{y}}_t^k = \mathcal{A}_{A^t, \mathbf{S}^k}(\mathbf{x}_t^*) + \tilde{\mathbf{e}}_t^k, \quad \mathcal{A}_{A^t, \mathbf{S}^k} := \mathbf{U}_{A^t} \mathcal{F} \mathbf{S}^k, \quad k = 1, \dots, n_c, \quad t = 1, \dots, n_f, \quad (1)$$

where  $\mathbf{U}_M$  denotes a subsampling operator acting on a set  $M \subseteq \Omega$  as follows:

$$\mathbf{z}_M : (\mathbf{z}_M)_i = (\mathbf{U}_M \mathbf{z})_i = \mathbf{z}_i \cdot \mathbb{1}_M(i), \quad i \in \Omega, \quad \mathbf{z} \in \mathbb{C}^{n \times n_c}. \quad (2)$$

Here,  $\Omega := \{1, 2, \dots\}$  denotes the sample space comprising all possible sampling options, where  $|\Omega|$  equals  $n_2$  or  $n$  for 1D (column) sampling and 2D (point) sampling, respectively.  $\mathcal{F}$  denotes the forward FFT,  $\mathbf{S}^k \in \mathbb{C}^{n \times n}$  the sensitivity map of the  $k$ -th coil, and  $\mathbf{e}_t^k$  measurement noise. The acceleration factor (AF) of the acquisition of  $\tilde{\mathbf{y}}$  is determined by the dynamic acquisition set  $A = \{A^t\}_{t=1}^{n_f} \subset \Omega^{n_f}$ :  $\text{AF} = \frac{n_f |\Omega|}{\sum_{t=1}^{n_f} |A^t|}$ , where  $|\cdot|$  denotes the cardinality.

The goal of dynamic MRI reconstruction involves obtaining an approximation of  $\mathbf{x}^*$  using  $\tilde{\mathbf{y}}$ , formulated as a regularized least-squares optimization problem [4]:

$$\hat{\mathbf{x}} = \underset{\mathbf{x} \in \mathbb{C}^{n \times n_f}}{\operatorname{argmin}} \frac{1}{2} \sum_{t=1}^{n_f} \sum_{k=1}^{n_c} \left\| \mathcal{A}_{A^t, \mathbf{S}^k}(\mathbf{x}_t) - \tilde{\mathbf{y}}_t^k \right\|_2^2 + \mathcal{G}(\mathbf{x}), \quad (3)$$

where  $\mathcal{G} : \mathbb{C}^{n \times n_f} \rightarrow \mathbb{R}$  represents an arbitrary regularization functional imposing prior reconstruction information.

Our objectives in this project involve learning an adaptive dynamic sampling pattern  $\mathbf{U}_A := (\mathbf{U}_{A^1}, \dots, \mathbf{U}_{A^{n_f}})$  that maximizes the information content of the acquired subsampled data  $\tilde{\mathbf{y}}$  which is adapted based on some initial dynamic  $k$ -space data  $\tilde{\mathbf{y}}_{A_0}$ , and within the same framework train a DL-based dynamic reconstruction technique. The idea is that both sampling and reconstruction are improved and co-trained by exploiting cross-frame information found across the dynamic data.

### 2.2 Sensitivity Map Prediction

Coil sensitivities are estimated using the fully-sampled central  $k$ -space region, or autocalibration signal (ACS). This is further refined by a 2D U-Net-based [22] Sensitivity Map Predictor (SMP),  $\mathcal{S}_\omega$ , an approach proven effective in enhancing sensitivity map prediction [25, 18, 37].

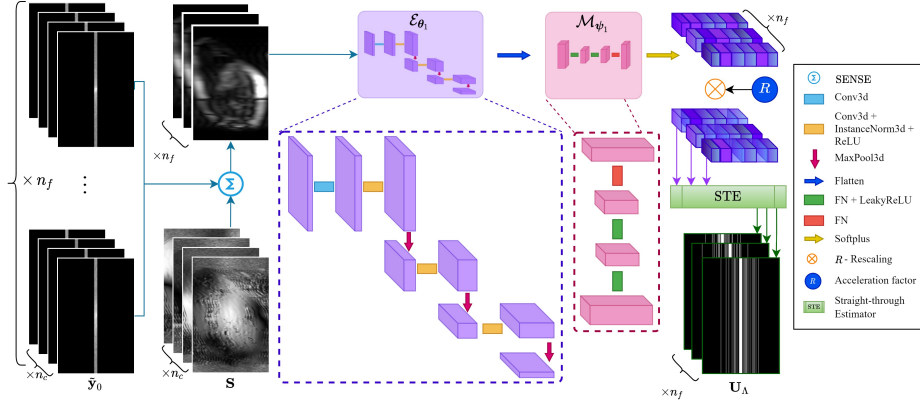


Fig. 1: Overview of the Adaptive Dynamic Sampler for frame-specific  $k$ -space sampling. Initial multi-coil dynamic  $k$ -space measurements  $\tilde{\mathbf{y}}_0$  and sensitivity maps  $\mathbf{S}$  are used to perform a SENSE reconstruction, which serves as the input to the encoder  $\mathcal{E}_{\theta_1}$  in the ADS module. The encoder output is flattened and passed to a multi-layer perceptron  $\mathcal{M}_{\psi_1}$ , which generates probability vectors for each potential sampling location. These probabilities are softplused, rescaled to meet the acceleration factor  $R$ , and binarized using a straight-through estimator layer to produce the sampling pattern  $\mathbf{U}_A$ , ensuring  $\text{AF}(\mathcal{A}) = R$ . For brevity here we assume that  $\tilde{\mathbf{y}}_0$  comprises only of ACS data and we also assume only a single ADS cascade ( $N = 1$ ).

### 2.3 Adaptive Dynamic Sampler

To adapt the subsampling pattern to each case, we introduce the Adaptive Dynamic Sampler (ADS), extending a previous approach for static adaptive sampling [3] trained jointly with a variational network reconstruction model [25]. Given initial measurements  $\tilde{\mathbf{y}}_0 \in \mathbb{C}^{n \times n_c \times n_f}$  acquired from an initial set  $\Lambda_0 \subset \Omega^{n_f}$  (e.g.,  $\Lambda_0 = \Lambda_{\text{acs}}$ ), ADS allocates a sampling budget online:  $\mathbf{n}_b = (n_b^1, \dots, n_b^{n_f}) = (\frac{n_a}{R} - |\Lambda_0^1|, \dots, \frac{n_a}{R} - |\Lambda_0^{n_f}|)$ . Here,  $n_a = |\Omega|$  denotes the total number of potential samples, and  $R$  an arbitrary acceleration factor. We focus on frame-specific sampling (for unified set  $n_f = 1$ ).

ADS operates through a number of  $N$  cascades, dividing the sampling budget evenly as  $\frac{\mathbf{n}_b}{N}$  across cascades. Each cascade comprises an encoder module  $\mathcal{E}_{\theta_m}$  and a multi-layer perceptron (MLPs)  $\mathcal{M}_{\psi_m}$ . The encoders follow a U-Net [22] encoder structure, alternating between  $l_{\text{enc}}$  3D convolutional layers ( $3^3$  kernels) with instance normalization [28] and ReLU [32] activations, and max-pooling layers ( $2^3$  kernels), except for the first layer. MLPs consist of  $l_{\text{mlp}}$  linear layers, with leaky ReLU [32] (with negative slope 0.01) activation, except for the final layer.

Each  $\mathcal{E}_{\theta_m}$  receives (subsampling) multi-coil  $k$ -space measurements as input, which are reconstructed into a single image via complex conjugate sensitivity map sum (SENSE reconstruction). The resulted image is subsequently flattened



and introduced into  $\mathcal{M}_{\psi_m}$ , generating probability vectors  $\mathbf{p}_m = (\mathbf{p}_m^1, \dots, \mathbf{p}_m^{n_f}) \in \mathbb{R}^{n_f \times n_a}$  such that  $\mathbf{p}_m^t \in \mathbb{R}^{n_a}$ . Probabilities in  $\mathbf{p}_m^t$  corresponding to previously acquired measurements on  $\bigcup_{j=0}^{m-1} \Lambda_j^t$  are set to zero. A softplus activation function is applied to each  $\mathbf{p}_m^t$ , followed by rescaling (see Algorithm A1 in Appendix A) to ensure  $\mathbb{E}(\mathbf{p}_m^t) = \frac{n_b^t}{N \times n_a}$ .

To enable differentiability of the binarization process and allow end-to-end training, we apply a straight-through estimator [38] (STE) for gradient approximation, following prior work [3, 39, 42]. This stochastically generates  $\Lambda_m^t$  by binarizing  $\mathbf{p}_m^t$  through rejection sampling to meet the sampling budget  $\frac{n_b}{N}$ , with gradients approximated using a sigmoid function (slope = 10). The STE’s forward and backward passes are detailed in Algorithms A2 and A3 (Appendix A), with further details in Appendix B.

The first ADS cascade processes the initial data  $\tilde{\mathbf{y}}_0$ , and each subsequent cascade  $m$  takes as input  $k$ -space data  $\tilde{\mathbf{y}}_{m-1}$  produced from the previous cascade aiming to produce a new acquisition set  $\Lambda_m = (\Lambda_m^1, \dots, \Lambda_m^{n_f}) \subset \Omega^{n_f}$ , ensuring  $\Lambda_{m-1}^t \cap \Lambda_m^t = \emptyset$  and  $|\Lambda_m^t| = \frac{n_b^t}{N} + |\Lambda_0^t|$ . The new  $k$ -space data is then acquired from the predicted set  $\Lambda_m$  as  $\mathbf{U}_{\Lambda_m} \mathbf{y} = (\mathbf{U}_{\Lambda_m^1} \mathbf{y}^1, \dots, \mathbf{U}_{\Lambda_m^{n_f}} \mathbf{y}^{n_f})$ , which is subsequently aggregated with previous data, equivalent to an acquisition on  $\bigcup_{j=0}^m \Lambda_j$ :

$$\tilde{\mathbf{y}}_m := \tilde{\mathbf{y}}_{m-1} + \mathbf{U}_{\Lambda_m} \mathbf{y} \iff \tilde{\mathbf{y}}_m = \mathbf{U}_{\bigcup_{j=0}^m \Lambda_j} \mathbf{y}. \quad (4)$$

This sequential approach yields the final set  $\Lambda := \bigcup_{m=0}^N \Lambda_m \subset \Omega^{n_f}$  satisfying  $|\Lambda| = \sum_{m=1}^N \sum_{t=1}^{n_f} |\Lambda_m^t| = n_f \times \frac{n_a}{R}$ , ensuring  $\text{AF}(\Lambda) = R$ . See Figure 1 for a depiction of the ADS module, with further details in Algorithms A4 and A5 in Appendix A.

## 2.4 Dynamic MRI Reconstruction

Our proposed pipeline (Section 2.5) is independent of the specific reconstruction method employed. To demonstrate this flexibility and robustness, we incorporate two state-of-the-art (SOTA) reconstruction models: the variable Splitting Half-quadratic ADMM algorithm for Reconstruction of inverse-Problems (vSHARP) [35, 34] and the Model-based neural network with Enhanced Deep Learned regularizers (MEDL-Net) [20].

We primarily employ vSHARP due to its demonstrated SOTA performance, particularly in the CMRxRecon Challenge 2023 for dynamic cardiac MRI reconstruction. It efficiently solves (3) by employing half-quadratic variable splitting and applies ADMM-unrolled optimization over  $T$  iterations. To assess the robustness of our pipeline with different reconstruction models, we also integrate MEDL-Net, which is also designed to solve (3) iteratively. By incorporating dense connections between iteration cascades, MEDL-Net reduces the number of required cascades while maintaining reconstruction quality.

Given subsampled measurements  $\tilde{\mathbf{y}}$  and sensitivity maps  $\mathbf{S}$ , the reconstruction model predicts the underlying dynamic image:  $\hat{\mathbf{x}} = \mathcal{R}_\phi(\tilde{\mathbf{y}}; \mathbf{S})$ . Further details

can be found in the literature [35,34,20]. Other dynamic MRI reconstruction approaches, such as [43,10,13], have employed methods ranging from compressed sensing to deep learning-based spatiotemporal modeling.

## 2.5 End-to-end Adaptive Dynamic Sampling and Reconstruction

For our end-to-end approach to adaptive dynamic subsampling and reconstruction we integrate the methodologies detailed in Sections 2.2, 2.3, and 2.4. The process is visually summarized in Figure 2 and algorithmically in Algorithm A6 in Appendix A. Given ACS data  $\hat{\mathbf{y}}_{\text{acs}}$ , the sensitivities  $\mathbf{S}$  are predicted via  $\mathcal{S}_{\omega}$ . Subsequently, with initial measurements  $\hat{\mathbf{y}}_0$  and a specified acceleration factor  $R$ , the adaptive dynamic sampling module  $\text{ADS}_{\psi,\theta}$  generates an adaptive dynamic subsampling pattern  $\mathbf{U}_\Lambda$ , where  $\Lambda$  is as defined in Section 2.3. Note that for acceleration consistency we choose  $\Lambda_{\text{acs}} \subseteq \Lambda_0$ . After acquiring the data  $\hat{\mathbf{y}}_\Lambda$  using  $\mathbf{U}_\Lambda$ ,  $\mathcal{R}_\phi$  produces a dynamic image reconstruction utilizing  $\mathbf{S}$  and  $\hat{\mathbf{y}}_\Lambda$ .

The training of our framework proceeds in an end-to-end manner, ensuring gradients propagate effectively across all three modules, allowing for simultaneous optimization of sampling and reconstruction. The ADS module, as detailed in Section 2.2, employs a STE to approximate gradients through the binarization process, ensuring differentiability and enabling reconstruction loss gradients to flow back through the ADS module. The co-optimization of ADS with SMP and the reconstruction model is achieved through loss computation at the end of the forward pass of the pipeline. In this design, the reconstruction network processes adaptively sampled measurements, and the resulting reconstruction loss (see Section 2.6 for how we calculate loss) propagates supervision signals throughout the pipeline. This joint optimization ensures that both the sampling patterns and reconstruction quality are systematically improved. Implemented in PyTorch [17], the framework leverages its automatic differentiation capabilities to compute gradients seamlessly across all components, including the probabilistic sampling steps within ADS.

## 2.6 Experiments

**Dataset** We utilized the CMRxRecon dataset [31], comprising 473 scans of 4D (in total 3185 2D sequences) multi-coil cine cardiac  $k$ -space data, split into training, validation, and test sets (251, 111, 111 scans, respectively). For more details refer to Appendix B.

**Comparative & Ablation Studies** To validate our proposed E2E-ADS-Recon, particularly with respect to adaptive sampling, we evaluate various sampling strategies under both frame-specific and unified settings:

### 1. Learned:

- (a) Our pipeline employing different initializations: (i) ACS-initiated ( $\Lambda_0 = \Lambda_{\text{acs}}$ ) (Adpt-AcsInit), (ii) equispaced with  $\frac{|\Omega|}{|\Lambda_0|} = R - 4$  (Adpt-EqInit-I),

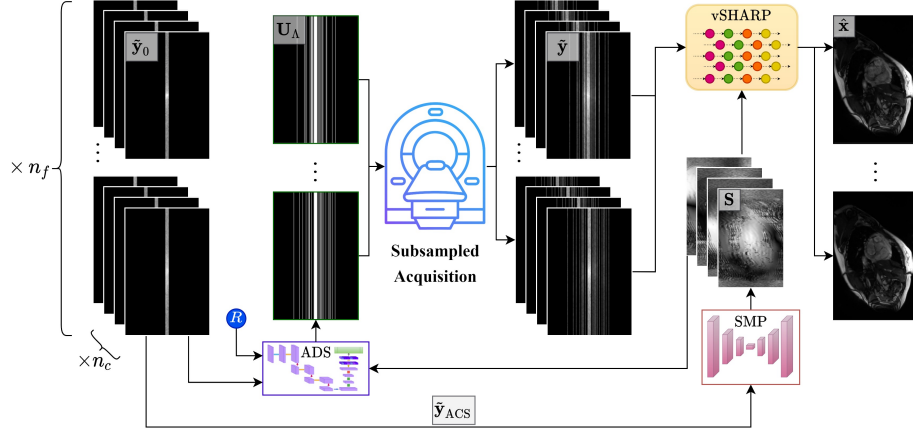


Fig. 2: Overview of the E2E-ADS-Recon pipeline or frame-specific  $k$ -space sampling. Initial multi-coil dynamic  $k$ -space measurements  $\tilde{\mathbf{y}}_0$  include ACS data  $\tilde{\mathbf{y}}_{\text{ACS}}$ , which are used by the SMP module to generate coil sensitivity maps  $\mathbf{S}$ . These sensitivity maps and the initial measurements are input to the ADS module, which generates adaptive sampling patterns  $\mathbf{U}_A$  based on the desired acceleration factor  $R$ . These patterns guide subsampled  $k$ -space acquisitions during dynamic imaging. The subsampled data  $\tilde{\mathbf{y}}$  are processed with the sensitivity maps  $\mathbf{S}$  in the reconstruction module (e.g., vSHARP), yielding reconstructions  $\hat{\mathbf{x}}$ . The pipeline, including ADS, SMP and reconstruction model, is jointly optimized end-to-end to enhance imaging quality. For simplicity, the illustration assumes a single ADS cascade ( $N = 1$ ).

- (iii)  $\frac{|\Omega|}{|\Lambda_0|} = R - 2$  (Adpt-EqInit-II), and (iv)  $kt$ -equispaced with  $\frac{|\Omega|}{|\Lambda_0|} = R - 2$  (Adpt- $kt$ EqInit-II). For configurations (ii)-(iv),  $\Lambda_{\text{acs}} \subset \Lambda_0$ , and these are applicable only to 1D sampling.
  - (b) Non-adaptive optimized learned schemes, where the sampling space is parameterized and optimized end-to-end with the reconstruction model [1] (Opt).
- 2. Predetermined/Random:**
- (a) Common non-adaptive schemes, including (i) 1D random uniform (Rand), (ii) 1D Gaussian (Gauss-1D), (iii) 2D equispaced (Equi), (iv) 2D Gaussian (Gauss-2D), and (v) radial (Rad) trajectories [36]. In frame-specific experiments, a unique trajectory was used for each frame, whereas in unified settings, the same pattern was applied across all frames.
  - (b) Non-adaptive schemes with temporal interleaving, also known as  $kt$  schemes [26], including  $kt$ -equispaced ( $kt$ Equi),  $kt$ -Gaussian 1D ( $kt$ Gauss-1D) and  $kt$ -radial ( $kt$ Rad).

We provide more information for these schemes in Appendix B. For non-adaptive methods, we replace the ADS with each sampling strategy while keeping the rest of the architecture (SMP and reconstruction model) unchanged.

We also conduct ablation studies on the E2E-ADS-Recon model with the following variations:

1. A modified version of our proposed method using a single cascade for ADS ( $N = 1$ ) instead of two, as in the comparative studies, also employing different initializations.
2. Non-uniform sampling budget allocation across time frames in the ADS module (Adpt-NU), compared to equal division used in the original framework (applicable only in frame-specific settings).

## Experimental Setup

*Optimization* Models were developed in PyTorch [17], using the Adam optimizer [11] with a learning rate starting at 1e-3, linearly increasing to 3e-3 over 2k iterations, then reducing by 20% every 10k iterations, over 52k iterations. Experiments were conducted on single A6000 or A100 NVIDIA GPUs, with a batch size of 1. We used a dual-domain loss strategy [35], combining image and frequency domain losses:

$$\mathcal{L} = \sum_{j=1}^T w_j \left[ \sum_{t=1}^{n_f} (\mathcal{L}_{\text{SSIM}}(\hat{\mathbf{x}}_t^{(j)}, \mathbf{x}_t^*) + \mathcal{L}_1(\hat{\mathbf{x}}_t^{(j)}, \mathbf{x}_t^*) + \mathcal{L}_{\text{HFEN}}(\hat{\mathbf{x}}_t^{(j)}, \mathbf{x}_t^*)) + \mathcal{L}_{\text{SSIM3D}}(\hat{\mathbf{x}}^{(j)}, \mathbf{x}^*) \right] + 3 \cdot \mathcal{L}_{\text{NMAE}}(\hat{\mathbf{y}}, \mathbf{y}), \quad w_j = 10^{(j-T)/(T-1)}, \quad (5)$$

where  $\{\hat{\mathbf{x}}^{(j)}\}_{j=1}^T$  denotes the predicted dynamic images from vSHARP’s unrolled steps, and  $\hat{\mathbf{y}}$  represents the predicted  $k$ -space data. The choice of individual loss components and their respective weights follows the training protocol of the vSHARP applied to the CMRxRecon challenge 2023 [35,34,16]. The definitions of each component can be found in the literature [34].

*Hyperparameter Settings* In our adaptive sampling experiments, we configured the ADS sampler with  $N = 2$  cascades. Unless specified otherwise, we use image domain encoding ADS modules. Our setup features encoders with  $l_{\text{enc}} = 3$  scales and MLPs with  $l_{\text{mlp}} = 3$  layers each.

In all our experiments the SMP module comprised a 2D U-Net with 4 scales (16, 32, 64, 128 channels) and we used vSHARPs [34] with  $T = 8$  and 3D U-Nets as denoisers composed of 4 scales (16, 32, 64, 128 channels).

*Reconstruction Model Robustness* We repeat the (frame-specific) comparative studies outlined in Section 2.6 using MEDL-Net [20] as the reconstruction model instead of vSHARP to explore the robustness of our end-to-end pipeline. Optimization and hyperparameter choice details are specified in Appendix B.

*Subsampling* All experiments (learned or otherwise) used a fraction  $r_{\text{acs}} := |\Lambda_{\text{acs}}| = 4\%$  of  $\Omega$  to fully sample the  $k$ -space center, denoted as  $\tilde{\mathbf{y}}_{\Lambda_{\text{acs}}}$ , which is used for sensitivity map prediction, similar to the literature [25,18,37]. In learned sampling experiments,  $\Lambda_0 = \Lambda_{\text{acs}}$ , unless stated otherwise. During training the acceleration was randomly chosen between  $4\times, 6\times, 8\times$ , while for inference we evaluated each setups on acceleration factors of  $4\times, 6\times$  and  $8\times$ .

*Evaluation* The models were assessed using SSIM, PSNR, and NMSE metrics, as defined in the literature [36]. These metrics were averaged per slice or frame within each scan, after being centrally cropped (region of interest, ignore background) to two-thirds of each dimension. For significance testing, we use the almost stochastic order test [5,27] with  $\alpha = 0.05$ .

### 3 Results

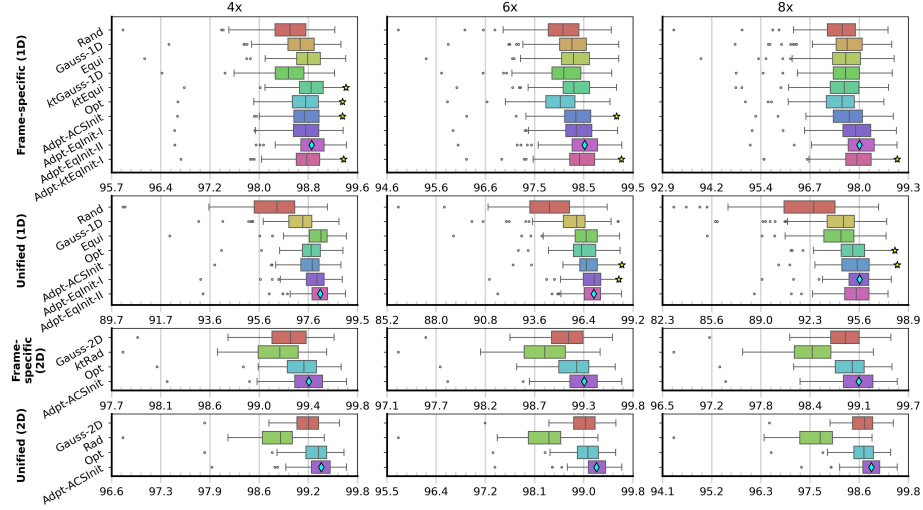


Fig. 3: SSIM ( $\times 100$ ) metrics across all experimental settings and setups. Diamonds ( $\diamond$ ) on the box-plot median indicate the average best methods. A star ( $\star$ ) on the upper whisker indicates non-significance in comparison to the average best method.

Quantitative analysis is presented in Figure 3, C1 and C2, which display the distributions of SSIM, PSNR, and NMSE metrics for the test set. Boxplots highlight the top-performing methods and their statistical significance across all configurations.

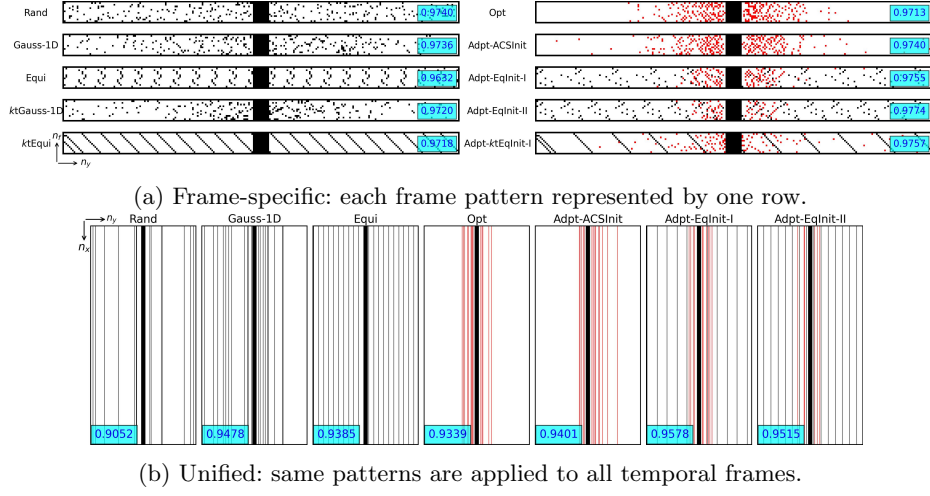


Fig. 4: Examples of 1D patterns across setups at  $R = 8$  for (a) frame-specific and (b) unified settings. Black: fixed/initial, red: learned pattern. Cyan boxes mark SSIM values.

Our results consistently demonstrate that frame-specific sampling outperforms unified sampling across all tested configurations, acceleration factors, and sampling dimensions (line-1D point-2D).

Among the methods evaluated, our proposed E2E-ADS-Recon achieves the highest performance across nearly all combinations of frame-specific and unified setups, for both 1D and 2D sampling. E2E-ADS-Recon shows statistically significant results in most metrics, with the highest SSIM values achieved by variants of our approach. A similar trend is observed for PSNR and NMSE, although in frame-specific 1D sampling at  $R = 4$ , equispaced sampling slightly outperforms our method.

For 1D sampling, both frame-specific and unified setups benefit from combining our adaptive strategy with equispaced initialization and ACS  $k$ -space data, yielding the highest average performance. Despite this, non-adaptive equispaced sampling remains the top competitor. At high acceleration factors ( $6\times, 8\times$ ), all ADS configurations generally outperform non-adaptive methods in both frame-specific and unified settings concerning the SSIM metric, and this pattern is also observed for PSNR and NMSE in most cases.

In 2D setups, E2E-ADS-Recon significantly surpasses non-adaptive methods across all metrics and acceleration factors, with optimized parameterized sampling being the closest competitor.

Qualitative results are shown in Figure 4, which shows examples of generated 1D sampling patterns for both setups. Visual inspection of generated sampling patterns reveals that learned patterns tend to prioritize lower-frequency components near the  $k$ -space center, while occasionally incorporating higher fre-

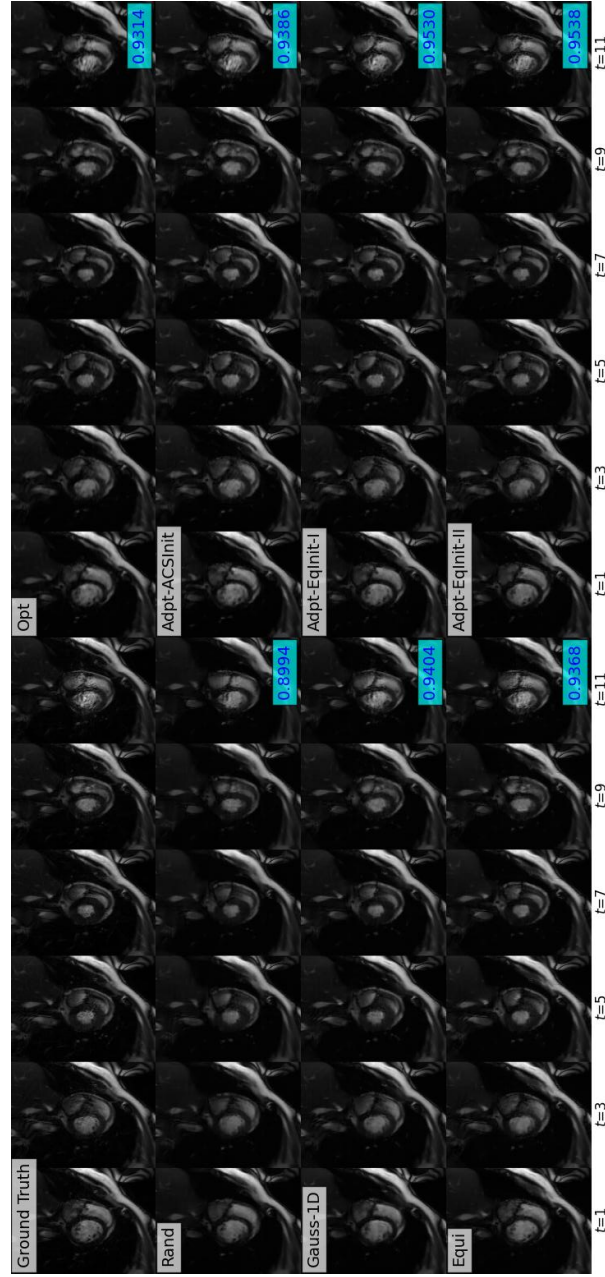


Fig. 5: Example of reconstructions across setups for unified 1D sampling at  $R = 8$ .



quencies. In Figure 5, we illustrate example reconstructions from the unified experiments at a high acceleration factor ( $R = 8$ ), where adaptive methods demonstrate improved preservation of anatomical structures and reduced artifacts relative to non-adaptive approaches. Additional pattern examples and image reconstructions for all setups are available in Appendix D.

Tables C1 and C2 provide results from our ablation study employing single ( $N = 1$ ) ADS cascade, as well as non-uniform frame-specific adaptive sampling. Using a single, instead of two, cascades yields performance comparable to using two cascades, with most cases outperforming non-adaptive methods. On the other hand, non-uniform sampling budget allocation did not show competitive results compared to equal budget distribution across time frames.

*Reconstruction Model Robustness* Additional results are provided in Appendix C, where we replace the reconstruction model with MEDL-Net. Figures C3, C4, and C5 present the corresponding SSIM, PSNR, and NMSE metrics. Across both 1D and 2D sampling, the numerical trends remain consistent with those observed using vSHARP as the reconstruction module. In nearly all acceleration-metric combinations, adaptive sampling methods outperform their non-adaptive counterparts on average, except for SSIM at  $R = 4$ , where the *ktEqui* scheme shows a slight, though statistically insignificant, advantage. For 1D sampling, E2E-ADS-Recon with equispaced initialization continues to be the top-performing configuration in most cases. Furthermore, the benefits of adaptive sampling become more evident at higher acceleration factors (e.g.,  $R = 8$ ). Additionally, while not the primary focus of this study, we observe that employing vSHARP yields overall better results than MEDL-Net.

## 4 Discussion

In this work, we introduced E2E-ADS-Recon (End-to-End Adaptive Dynamic Subsampling and Reconstruction), integrating a deep learning-based adaptive sampler for dynamic MRI accelerated acquisition with state-of-the-art reconstruction networks for dynamic reconstruction. E2E-ADS-Recon is trained end-to-end to produce online adaptive, case-specific dynamic acquisition patterns for any given acceleration factor, followed by dynamic image reconstruction, effectively exploiting temporal correlations between temporal frames.

We evaluated E2E-ADS-Recon using 4D fully-sampled cine cardiac MRI data under two sampling settings: frame-specific (distinct subsampling patterns per time frame to exploit inter-frame correlations) and unified (the same pattern applied across all frames). We also considered two sampling dimensions: 1D (line) and 2D (point). Our approach was benchmarked against equivalent pipelines that replaced the adaptive sampler of E2E-ADS-Recon with other various non-adaptive sampling schemes, including common 1D or 2D schemes (random, equispaced, Gaussian, radial), as well as data-optimized approaches.

Visualization of the sampling patterns (see Figure 4 and Supplementary Material D) generated by E2E-ADS-Recon revealed that the ADS component consistently produced adaptive patterns with denser sampling in the lower frequency



regions (closer to the  $k$ -space center) which contain a structural information and image contrast information, while occasionally sampling higher frequencies. In addition, the visualizations show that in frame-specific sampling experiments, the ADS module learned to generate distinct patterns for each temporal frame. As a result, this allowed the reconstruction model to effectively leverage complementary information across frames and produce better reconstructions in compared to the unified setting.

Even though the performance improvements observed with E2E-ADS-Recon may appear incremental, they are statistically significant. Reporting such improvements is a common practice in MRI literature, where the focus often lies on incremental yet meaningful enhancements (e.g., close performance of top teams in CMRxRecon Challenge 2023 [16]). The relatively modest gains in reconstruction quality are partially attributed to the powerful vSHARP model used, which inherently minimizes the impact of different sampling patterns. Nonetheless, the consistent performance gains across experiments highlight the potential of adaptive sampling, particularly at higher acceleration rates.

Additionally, we replaced the vSHARP model with another state-of-the-art method (MEDL-Net) to assess the reconstruction model’s robustness. The results remained consistent, with adaptive sampling configurations continuing to outperform non-adaptive approaches across sampling dimensions and acceleration factors.

Despite the promising results of E2E-ADS-Recon, its supervised training requires fully-sampled data, similar to other data-optimized or adaptive sampling approaches, limiting its applicability to the availability of such data. Non-learned sampling methods, on the other hand, can leverage subsampled datasets for self-supervised learning of reconstruction models without requiring fully-sampled data. Recent studies have shown that joint supervised and self-supervised training of reconstruction models can enhance self-supervised results [33]. Future work could explore such direction to extend the applicability of E2E-ADS-Recon to datasets without fully-sampled  $k$ -spaces.

Another factor to consider is the use of initial data (e.g., ACS) in E2E-ADS-Recon. The ADS module relies on this initialization to generate adapted, case-specific acquisition, unlike optimized sampling methods that do not require pre-sampled data. This dependency on the initial sampling pattern is a limitation shared with methods requiring initial data for calibration, such as GRAPPA or RAKI, where the quantity and size of the initial data significantly affect downstream reconstruction [12]. Similarly, in learned adaptive sampling in static imaging scenarios, initialization with low-frequency (ACS) data is common, as seen in approaches employing reinforcement learning [19,2] or deep learning [39]. Additionally, the influence of different sampling patterns on reconstruction performance has been well-documented in prior studies [36,9]. In E2E-ADS-Recon, using ACS-reconstructed images for initialization is a natural choice, as these data are already required for sensitivity profile estimation in DL-based reconstruction methods [37].

While our retrospective study demonstrates the potential of E2E-ADS-Recon, practical implementation within an MRI scanner remains to be tested and is beyond the scope of this paper. Implementing such an end-to-end framework on a scanner might present significant complexities; however, this study represents an essential step toward jointly optimizing sampling and reconstruction. Importantly, the observed improvements, though incremental, suggest that adaptive sampling could yield meaningful gains in real-world applications.

Our results underscore the advantages of frame-specific sampling over unified strategies. Frame-specific methods, which employ distinct patterns per time frame, more effectively leveraged temporal correlations, resulting in higher reconstruction quality. However, practical challenges such as large gradient switches and eddy currents might arise with frame-specific schemes, whereas unified approaches are less likely to encounter these issues. Additionally, the implementation of frame-specific sampling requires knowledge of the anatomical phase at each moment to apply the correct sampling pattern. Finally, while our results indicate that 2D sampling outperforms 1D sampling consistently with previous studies [39,36], future studies should investigate the physical implementation and application of 2D sampling in a clinical setting.

## References

1. Bahadir, C.D., Dalca, A.V., Sabuncu, M.R.: Learning-Based Optimization of the Under-Sampling Pattern in MRI, p. 780–792. Springer International Publishing (2019). [https://doi.org/10.1007/978-3-030-20351-1\\_61](https://doi.org/10.1007/978-3-030-20351-1_61) 2, 7
2. Bakker, T., van Hoof, H., Welling, M.: Experimental design for mri by greedy policy search. *Advances in Neural Information Processing Systems* **33**, 18954–18966 (2020) 2, 13
3. Bakker, T., Muckley, M.J., Romero-Soriano, A., Drozdal, M., Pineda, L.: On learning adaptive acquisition policies for undersampled multi-coil MRI reconstruction. In: *Medical Imaging with Deep Learning* (2022) 2, 4, 5
4. Bertero, M.: Regularization methods for linear inverse problems. In: *Inverse Problems: Lectures given at the 1st 1986 Session of the Centro Internazionale Matematico Estivo (CIME) held at Montecatini Terme, Italy, May 28–June 5, 1986*, pp. 52–112. Springer (2006) 3
5. Dror, R., Shlomov, S., Reichart, R.: Deep dominance-how to properly compare deep neural models. In: *Proceedings of the 57th Annual Meeting of the Association for Computational Linguistics*. pp. 2773–2785 (2019) 9, 26
6. Gamper, U., Boesiger, P., Kozerke, S.: Compressed sensing in dynamic mri. *Magnetic Resonance in Medicine: An Official Journal of the International Society for Magnetic Resonance in Medicine* **59**(2), 365–373 (2008) 2
7. Gautam, S., Li, A., Ravishankar, S.: Patient-adaptive and learned mri data under-sampling using neighborhood clustering (2024) 2
8. Guo, P., Mei, Y., Zhou, J., Jiang, S., Patel, V.M.: Reconformer: Accelerated mri reconstruction using recurrent transformer. *IEEE transactions on medical imaging* (2023) 2
9. Hammernik, K., Knoll, F., Sodickson, D.K., Pock, T.: On the influence of sampling pattern design on deep learning-based mri reconstruction. In: *25th Scientific*

- Meeting and Exhibition of the International Society for Magnetic Resonance in Medicine: ISMRM 2017. p. 0644 (2017) [13](#)
10. Huang, Q., Xian, Y., Yang, D., Qu, H., Yi, J., Wu, P., Metaxas, D.N.: Dynamic mri reconstruction with end-to-end motion-guided network. *Medical Image Analysis* **68**, 101901 (2021) [6](#)
  11. Kingma, D.P.: Adam: A method for stochastic optimization. *arXiv preprint arXiv:1412.6980* (2014) [8](#)
  12. Knoll, F., Hammernik, K., Zhang, C., Moeller, S., Pock, T., Sodickson, D.K., Akcakaya, M.: Deep-learning methods for parallel magnetic resonance imaging reconstruction: A survey of the current approaches, trends, and issues. *IEEE Signal Processing Magazine* **37**(1), 128–140 (2020). <https://doi.org/10.1109/MSP.2019.2950640> [13](#)
  13. Küstner, T., Fuin, N., Hammernik, K., Bustin, A., Qi, H., Hajhosseiny, R., Masci, P.G., Neji, R., Rueckert, D., Botnar, R.M., et al.: Cinenet: deep learning-based 3d cardiac cine mri reconstruction with multi-coil complex-valued 4d spatio-temporal convolutions. *Scientific reports* **10**(1), 13710 (2020) [6](#)
  14. Lønning, K., Caan, M.W., Nowee, M.E., Sonke, J.J.: Dynamic recurrent inference machines for accelerated mri-guided radiotherapy of the liver. *Computerized Medical Imaging and Graphics* **113**, 102348 (2024) [2](#)
  15. Lustig, M., Donoho, D.L., Santos, J.M., Pauly, J.M.: Compressed sensing mri. *IEEE Signal Processing Magazine* **25**(2), 72–82 (2008). <https://doi.org/10.1109/MSP.2007.914728> [2](#)
  16. Lyu, J., Qin, C., Wang, S., Wang, F., Li, Y., Wang, Z., Guo, K., Ouyang, C., Tänzer, M., Liu, M., et al.: The state-of-the-art in cardiac mri reconstruction: Results of the cmrxrecon challenge in miccai 2023. *Medical Image Analysis* p. 103485 (2025) [8](#), [13](#)
  17. Paszke, A., Gross, S., Massa, F., Lerer, A., Bradbury, J., Chanan, G., Killeen, T., Lin, Z., Gimelshein, N., Antiga, L., et al.: Pytorch: An imperative style, high-performance deep learning library (2019) [6](#), [8](#), [26](#)
  18. Peng, X., Sutton, B.P., Lam, F., Liang, Z.P.: Deepsense: Learning coil sensitivity functions for sense reconstruction using deep learning. *Magnetic resonance in medicine* **87**(4), 1894–1902 (2022) [3](#), [9](#)
  19. Pineda, L., Basu, S., Romero, A., Calandra, R., Drozdal, M.: Active mr k-space sampling with reinforcement learning. In: Martel, A.L., Abolmaesumi, P., Stoyanov, D., Mateus, D., Zuluaga, M.A., Zhou, S.K., Racocceanu, D., Joskowicz, L. (eds.) *Medical Image Computing and Computer Assisted Intervention – MICCAI 2020*. pp. 23–33. Springer International Publishing, Cham (2020) [2](#), [13](#)
  20. Qiao, X., Huang, Y., Li, W.: Medl-net: A model-based neural network for mri reconstruction with enhanced deep learned regularizers. *Magnetic Resonance in Medicine* **89**(5), 2062–2075 (2023) [5](#), [6](#), [8](#), [26](#)
  21. Qin, C., Schlemper, J., Caballero, J., Price, A.N., Hajnal, J.V., Rueckert, D.: Convolutional recurrent neural networks for dynamic MR image reconstruction. *IEEE Transactions on Medical Imaging* **38**(1), 280–290 (jan 2019). <https://doi.org/10.1109/tmi.2018.2863670>, <https://doi.org/10.1109/tmi.2018.2863670> [2](#)
  22. Ronneberger, O., Fischer, P., Brox, T.: U-net: Convolutional networks for biomedical image segmentation. In: *Lecture Notes in Computer Science*. pp. 234–241. Springer International Publishing (2015). [https://doi.org/10.1007/978-3-319-24574-4\\_28](https://doi.org/10.1007/978-3-319-24574-4_28), [https://doi.org/10.1007/978-3-319-24574-4\\_28](https://doi.org/10.1007/978-3-319-24574-4_28) [3](#), [4](#)
  23. Shannon, C.: Communication in the presence of noise. *Proceedings of the IRE* **37**(1), 10–21 (1949). <https://doi.org/10.1109/JRPROC.1949.232969> [2](#)

24. Shor, T.: Multi PILOT: Feasible learned multiple acquisition trajectories for dynamic MRI. In: Medical Imaging with Deep Learning (2023) [2](#)
25. Sriram, A., Zbontar, J., Murrell, T., et al.: End-to-end variational networks for accelerated mri reconstruction. In: Lecture Notes in Computer Science. p. 64–73. Springer International Publishing (2020). [https://doi.org/10.1007/978-3-030-59713-9\\_7](https://doi.org/10.1007/978-3-030-59713-9_7), [http://dx.doi.org/10.1007/978-3-030-59713-9\\_7](http://dx.doi.org/10.1007/978-3-030-59713-9_7) [3](#), [4](#), [9](#)
26. Tsao, J., Boesiger, P., Pruessmann, K.P.: k-t blast and k-t sense: dynamic mri with high frame rate exploiting spatiotemporal correlations. *Magnetic Resonance in Medicine: An Official Journal of the International Society for Magnetic Resonance in Medicine* **50**(5), 1031–1042 (2003) [7](#)
27. Ulmer, D., Hardmeier, C., Frellsen, J.: deep-significance-easy and meaningful statistical significance testing in the age of neural networks. arXiv preprint arXiv:2204.06815 (2022) [9](#)
28. Ulyanov, D., Vedaldi, A., Lempitsky, V.: Improved texture networks: Maximizing quality and diversity in feed-forward stylization and texture synthesis. In: 2017 IEEE Conference on Computer Vision and Pattern Recognition (CVPR). pp. 4105–4113 (2017). <https://doi.org/10.1109/CVPR.2017.437> [4](#)
29. Van Gorp, H., Huijben, I., Veeling, B.S., Pezzotti, N., Van Sloun, R.J.G.: Active deep probabilistic subsampling. In: Meila, M., Zhang, T. (eds.) Proceedings of the 38th International Conference on Machine Learning. Proceedings of Machine Learning Research, vol. 139, pp. 10509–10518. PMLR (18–24 Jul 2021) [2](#)
30. Wang, C., Li, Y., Lv, J., Jin, J., Hu, X., Kuang, X., Chen, W., Wang, H.: Recommendation for cardiac magnetic resonance imaging-based phenotypic study: Imaging part. *Phenomics* **1**(4), 151–170 (jul 2021). <https://doi.org/10.1007/s43657-021-00018-x> [24](#)
31. Wang, C., et al.: Cmrrecon: An open cardiac mri dataset for the competition of accelerated image reconstruction (2023). <https://doi.org/10.48550/ARXIV.2309.10836> [2](#), [6](#), [24](#)
32. Xu, B.: Empirical evaluation of rectified activations in convolutional network. arXiv preprint arXiv:1505.00853 (2015) [4](#)
33. Yiasemis, G., Moriakov, N., Sánchez, C.I., Sonke, J.J., Teuwen, J.: Jssl: Joint supervised and self-supervised learning for mri reconstruction (2023) [13](#)
34. Yiasemis, G., Moriakov, N., Sonke, J.J., Teuwen, J.: Deep cardiac mri reconstruction with admm. In: International Workshop on Statistical Atlases and Computational Models of the Heart. pp. 479–490. Springer (2023) [2](#), [5](#), [6](#), [8](#), [24](#)
35. Yiasemis, G., Moriakov, N., Sonke, J.J., Teuwen, J.: vsharp: Variable splitting half-quadratic admm algorithm for reconstruction of inverse-problems. *Magnetic Resonance Imaging* **115**, 110266 (2025). <https://doi.org/https://doi.org/10.1016/j.mri.2024.110266>, <https://www.sciencedirect.com/science/article/pii/S0730725X24002479> [5](#), [6](#), [8](#)
36. Yiasemis, G., Sánchez, C.I., Sonke, J.J., Teuwen, J.: On retrospective k-space subsampling schemes for deep mri reconstruction. *Magnetic Resonance Imaging* **107**, 33–46 (2024) [2](#), [7](#), [9](#), [13](#), [14](#), [25](#)
37. Yiasemis, G., Sonke, J.J., Sánchez, C., Teuwen, J.: Recurrent variational network: A deep learning inverse problem solver applied to the task of accelerated mri reconstruction. In: Proceedings of the IEEE/CVF Conference on Computer Vision and Pattern Recognition (CVPR). pp. 732–741 (June 2022) [2](#), [3](#), [9](#), [13](#)
38. Yin, P., Lyu, J., Zhang, S., Osher, S., Qi, Y., Xin, J.: Understanding straight-through estimator in training activation quantized neural nets. arXiv preprint arXiv:1903.05662 (2019) [5](#)

39. Yin, T., Wu, Z., Sun, H., Dalca, A.V., Yue, Y., Bouman, K.L.: End-to-end sequential sampling and reconstruction for mri. arXiv preprint arXiv:2105.06460 (2021) [2](#), [5](#), [13](#), [14](#)
40. Yoo, J., Jin, K.H., Gupta, H., Yerly, J., Stuber, M., Unser, M.: Time-dependent deep image prior for dynamic mri. *IEEE Transactions on Medical Imaging* **40**(12), 3337–3348 (2021) [2](#)
41. Zhang, C., Caan, M., Navest, R., Teuwen, J., Sonke, J.: Radial-rim: accelerated radial 4d mri using the recurrent inference machine. In: *Proceedings of International Society for Magnetic Resonance in Medicine*. vol. 31 (2023) [2](#)
42. Zhang, J., Zhang, H., Wang, A., Zhang, Q., Sabuncu, M., Spincemaille, P., Nguyen, T.D., Wang, Y.: Extending loupe for k-space under-sampling pattern optimization in multi-coil mri (2020) [2](#), [5](#)
43. Zhang, J., Han, L., Sun, J., Wang, Z., Xu, W., Chu, Y., Xia, L., Jiang, M.: Compressed sensing based dynamic mr image reconstruction by using 3d-total generalized variation and tensor decomposition: kt tgv-td. *BMC Medical Imaging* **22**(1), 101 (2022) [6](#)

## Supplementary Material

### A Algorithms

#### A.1 Rescale

---

**Algorithm A1:** Rescale to Budget
 

---

```

1: Input:
2:   Predicted probabilities  $\mathbf{p} \in \mathbb{R}^{n_a}$ 
3:   Sampling budget budget
4: Output:
5:   Rescaled probabilities  $\mathbf{p}_{\text{rescaled}}$ 

6: 1. Compute Scaling Parameters
7:  $s \leftarrow \text{budget}/n_a$  {Calculate target sparsity}
8:  $\bar{p} \leftarrow \mathbb{E}(\mathbf{p})$  {Compute mean probability}
9:  $r \leftarrow s/\bar{p}$  {Scaling factor for each sample}
10:  $\beta \leftarrow (1 - s)/(1 - \bar{p})$  {Adjustment factor for non-scaled elements}

11: 2. Rescale Probabilities
12: if  $r \leq 1$  then
13:    $\mathbf{p}_{\text{rescaled}} \leftarrow \mathbf{p} \cdot r$  {Scale down to fit target sparsity}
14: else
15:    $\mathbf{p}_{\text{rescaled}} \leftarrow \mathbf{1} - (\mathbf{1} - \mathbf{p}) \times \beta$  {Adjust larger values while preserving distribution}
16: end if

17: Return  $\mathbf{p}_{\text{rescaled}}$  such that  $\mathbb{E}(\mathbf{p}_{\text{rescaled}}) = s$ 

```

---

## A.2 Straight-through Estimator

---

**Algorithm A2:** Forward Pass of Straight-through Estimator

---

```

1: Input:
2:   Rescaled Probability  $\mathbf{p} = (p^1, \dots, p^{n_f}) \in \mathbb{R}^{n_f \times n_a}$ 
3:   Tolerance  $\text{tol} = 1e - 3$ 
4: Output:
5:   Binarized pattern  $\mathbf{r}$ 

6: 1. Binarization Process
7: for  $t = 1$  to  $n_f$  do
8:   for each  $p_i^t$  in  $p^t$  do
9:     Initialize  $\pi_i \sim U(0, 1)$  {Generate random uniform probability for  $\pi_i$ }
10:     $r_i^t \leftarrow \mathbb{I}(p_i^t > \pi_i)$  {Set  $r_i^t = 1$  if  $p_i^t > \pi_i$ , otherwise  $r_i^t = 0$ }
11:   end for

12: 2. Adjustment Loop (if needed)
13: while  $|\mathbb{E}[r^t] - \mathbb{E}[p^t]| \geq \text{tol}$  do
14:   for each  $p_i^t$  in  $p^t$  do
15:      $\pi_i \sim U(0, 1)$  {Regenerate random uniform probability for  $\pi_i$ }
16:      $r_i^t \leftarrow \mathbb{I}(p_i^t > \pi_i)$  {Re-binarize  $p_i^t$  with the new  $\pi_i$ }
17:   end for
18: end while
19: end for

20: 3. Finalization
21:  $\mathbf{r} = (r^1, \dots, r^{n_f})$ 
22: Store  $\pi$  {Store  $\pi$  for backward pass}

23: Return  $\mathbf{r}$ 

{Note: For unified sampling, set  $n_f = 1$ }

```

---

---

**Algorithm A3:** Backward Pass of Straight-through Estimator

---

```

1: Input:
2:   Gradient of loss w.r.t. output  $\nabla \mathcal{L}$ 
3:   Input probability  $\mathbf{p}$ 
4:   Probability  $\boldsymbol{\pi}$  from forward pass
5:   Slope  $\text{slope} = 10$ 
6: Output:
7:   Gradient w.r.t. input vector  $\nabla \mathbf{p}$ 

8: 1. Compute Sigmoid Gradient
9:  $\mathbf{g} \leftarrow \frac{\text{slope} \cdot \exp(-\text{slope} \cdot (\mathbf{p} - \boldsymbol{\pi}))}{(1 + \exp(-\text{slope} \cdot (\mathbf{p} - \boldsymbol{\pi})))^2}$ 

10: 2. Compute Gradient w.r.t. Input
11:  $\nabla \mathbf{p} \leftarrow \mathbf{g} \cdot \nabla \mathcal{L}$  {Element-wise gradient computation}

12: Return  $\nabla \mathbf{p}$ 

    {Note: All operations are element-wise}

```

---



### A.3 Adaptive Dynamic Sampler

---

**Algorithm A4:** Adaptive Dynamic Sampling for Frame-specific Patterns

---

```

1: Input:
2:   Initial data  $\tilde{\mathbf{y}}_0 \in \mathbb{C}^{n \times n_c \times n_f}$ 
3:   Acceleration  $R$ , Sample Space  $\Omega$ 
4: Output:
5:   Acquired  $k$ -space data  $\tilde{\mathbf{y}}$  for  $R$ 

6: 1. Initialize Sampling Budget
7:  $n_a \leftarrow |\Omega|$ 
8: {Calculate total budget}
9:  $\mathbf{n}_b = (n_b^1, \dots, n_b^{n_f}) \leftarrow (\frac{n_a}{R} - |A_0^1|, \dots, \frac{n_a}{R} - |A_0^{n_f}|)$ 

10: 2. Iterative Adaptive Sampling
11: for  $m = 1$  to  $N$  do
12:    $\mathbf{p}_m \leftarrow \mathcal{M}_{\psi_m} \circ \mathcal{E}_{\theta_m}(\tilde{\mathbf{y}}_{m-1})$  {Produce adaptive probabilities  $\mathbf{p}_m \in \mathbb{R}^{n_f \times n_a}$ }
13:   for  $t = 1$  to  $n_f$  do
14:     for each  $i \in (\bigcup_{j=0}^{m-1} A_j^t)$  do
15:        $(\mathbf{p}_m^t)_i \leftarrow 0$  {Zero-out already sampled indices}
16:     end for
17:      $\mathbf{p}_m^t \leftarrow \text{Softplus}(\mathbf{p}_m^t)$  {Apply Softplus}
18:      $\mathbf{p}_m^t \leftarrow \text{Rescale}(\mathbf{p}_m^t; \text{budget} = n_b^t/N)$  {Rescale such that  $\mathbb{E}(\mathbf{p}_m^t) = \frac{n_b^t}{N \times n_a}$ }
19:      $A_m^t \leftarrow \text{STE}(\mathbf{p}_m^t)$  {Produce adaptive sampling}
20:   end for
21:    $A_m \leftarrow (A_m^1, \dots, A_m^{n_f})$ 
22:    $\mathbf{z}_m \leftarrow \mathbf{U}_{A_m} \mathbf{y}$  {Acquire new  $k$ -space on  $A_m$ }
23:    $\tilde{\mathbf{y}}_m \leftarrow \tilde{\mathbf{y}}_{m-1} + \mathbf{z}_m = \mathbf{U}_{\bigcup_{j=0}^{m-1} A_j} \mathbf{y}$  {Aggregate with previous data}
24: end for

25: 3. Finalization
26:  $\tilde{\mathbf{y}} \leftarrow \tilde{\mathbf{y}}_N$ 

27: Return  $\tilde{\mathbf{y}}$ 

```

{Note: Lines **6-7** ensure  $A_{m-1}^t \cap A_m^t = \emptyset$ , and line **9** ensures  $|A_m^t| = |A_0^t| + \frac{m \times n_b^t}{N}$ }

---

---

**Algorithm A5:** Adaptive Dynamic Sampling for Unified Patterns

---

```

1: Input:
2:   Initial data  $\tilde{\mathbf{y}}_0 \in \mathbb{C}^{n \times n_c \times n_f}$ 
3:   Acceleration  $R$ , Sample Space  $\Omega$ 
4: Output:
5:   Acquired  $k$ -space data  $\tilde{\mathbf{y}}$  for  $R$ 

6: 1. Initialize Sampling Budget
7:  $n_a \leftarrow |\Omega|$ 
8:  $n_b \leftarrow \frac{n_a}{R} - |\Lambda_0|$  {Calculate total budget}

9: 2. Iterative Adaptive Sampling
10: for  $m = 1$  to  $N$  do
11:    $\mathbf{p}_m \leftarrow \mathcal{M}_{\psi_m} \circ \mathcal{E}_{\theta_m}(\tilde{\mathbf{y}}_{m-1})$  {Produce adaptive probabilities  $\mathbf{p}_m \in \mathbb{R}^{n_a}$ }
12:   for each  $i \in \left(\bigcup_{j=0}^{m-1} \Lambda_j\right)$  do
13:      $(\mathbf{p}_m)_i \leftarrow 0$  {Zero-out already sampled indices}
14:   end for
15:    $\mathbf{p}_m \leftarrow \text{Softplus}(\mathbf{p}_m)$  {Apply Softplus}
16:    $\mathbf{p}_m \leftarrow \text{Rescale}(\mathbf{p}_m; \text{budget} = n_b/N)$ 
17:   {Rescale such that  $\mathbb{E}(\mathbf{p}_m) = \frac{n_b}{N \times n_a}$ }
18:    $\Lambda_m \leftarrow \text{STE}(\mathbf{p}_m)$  {Produce adaptive sampling}
19:    $\Lambda_m \leftarrow (\Lambda_m, \dots, \Lambda_m)$  {Apply same pattern across frames}
20:    $\mathbf{z}_m \leftarrow \mathbf{U}_{\Lambda_m} \mathbf{y}$  {Acquire new  $k$ -space on  $\Lambda_m$ }
21:    $\tilde{\mathbf{y}}_m \leftarrow \tilde{\mathbf{y}}_{m-1} + \mathbf{z}_m = \mathbf{U}_{\bigcup_{j=0}^m \Lambda_j} \mathbf{y}$ 
22:   {Aggregate with previous data}
23: end for

24: 3. Finalization
25:  $\tilde{\mathbf{y}} \leftarrow \tilde{\mathbf{y}}_N$ 

26: Return  $\tilde{\mathbf{y}}$ 

```

{Note: Lines **5-6** ensure  $\Lambda_{m-1} \cap \Lambda_m = \emptyset$ , and line **8** ensures  $|\Lambda_m| = |\Lambda_0| + \frac{m \times n_b}{N}$ }

---

#### A.4 End-to-end Adaptive Dynamic Subsampling and Reconstruction

---

**Algorithm A6:** End-to-end Adaptive Dynamic Sampling and Reconstruction

---

```

1: Input:
2:   Initial data  $\tilde{\mathbf{y}}_{A_0}$ 
3:   ACS data  $\tilde{\mathbf{y}}_{A_{acs}} : A_{acs} \subseteq A_0$ 
4:   Acceleration factor  $R$ 
5: Output:
6:   Reconstructed image  $\hat{\mathbf{x}}$ 

7: 1. Estimate Sensitivity Maps
8: for  $k = 1$  to  $n_c$  do
9:   for  $t = 1$  to  $n_f$  do
10:     $\mathbf{S}_t^k \leftarrow \mathcal{S}_\omega(\tilde{\mathbf{y}}_{A_{acs}}^k)$  {Estimate sensitivity maps}
11:   end for
12: end for

13: 2. Adaptive Dynamic Sampling
14:  $\tilde{\mathbf{y}} \leftarrow \text{ADS}_{\psi, \theta}(\tilde{\mathbf{y}}_{A_0}; \mathbf{S}, R)$  {Adaptively sample  $k$ -space based on  $\tilde{\mathbf{y}}_{A_0}$  and  $R$ }

15: 3. Reconstruction
16:  $\hat{\mathbf{x}} \leftarrow \mathcal{R}_\phi(\tilde{\mathbf{y}}; \mathbf{S})$  {Reconstruct dynamic image}

17: Return  $\hat{\mathbf{x}}$ 

```

---

## B Additional Information

### B.1 Methods

**Straight-through Estimator** In the ADS component of our proposed method, we employ a straight-through estimator (STE) to binarize the predicted probabilities, which have been rescaled to the acceleration factor and zeroed out at already sampled locations. This is key for generating a binary mask from continuous probability values. The STE employs random uniform sampling in the forward pass, where each predicted probability is compared against a randomly drawn value from a uniform distribution (see Algorithm A2). This step is crucial for backpropagation because it allows the estimator to handle the non-differentiable nature of binarization. If a deterministic method like the top-k operator was used, the hard thresholding would result in non-differentiable operations, blocking gradient flow. By using random sampling, we create a smoother decision boundary that the STE can approximate during the backward pass with a sigmoid function.

Note that this stochasticity not only introduces randomness during training but also allows the model to better simulate real-world scenarios where decisions

are not always deterministic. Additionally, the stochastic nature of binarization is used during inference to maintain variability in the binary decision-making process.

In the backward pass (see Algorithm A3), the STE approximates the non-differentiable binarization step with a sigmoid function that has a slope of 10, enabling gradients to propagate through the discrete sampling operation. This allows for end-to-end training via backpropagation. Without this smooth approximation, gradients would vanish due to the hard thresholding, preventing effective learning.

**Handling Complex-Valued Operations** Complex-valued data, including images,  $k$ -space data, and sensitivity maps, were decomposed into their real and imaginary components, then stacked along the channel dimension (with size 2) for processing by real-valued model weights. As a result, all model weights were real-valued. Operations like the Fourier transform and its inverse were applied by temporarily converting the data back to its complex form when required.

## B.2 Experimental Setup

**Dataset** As outlined in Section 2.6, we used the cine CMRxRecon challenge 2023 dataset [31,30]. Specifically, the data were acquired using a 3T MRI scanner with a ‘TrueFISP’ readout. The dataset includes short-axis (SA), two, three and four-chamber long-axis (LA) views. Each scan consists of fully-sampled (ECG-triggered acquisition) multi-coil acquisitions ( $n_c = 10$ ) with 3-12 dynamic (2D + time) slices. The cardiac cycle was segmented into  $n_f = 12$  temporal phases (referred to as frames in the paper), with a temporal resolution of 50 ms. The spatial resolution was  $2.0 \times 2.0 \text{ mm}^2$ , with a slice thickness of 8.0 mm and a slice gap of 4.0 mm.

**Loss Function Definitions** This study utilizes multiple loss components derived from established literature. Specifically, we employ the image-domain losses  $\mathcal{L}_{\text{SSIM}} := 1 - \text{SSIM}$ ,  $\mathcal{L}_{\text{SSIM3D}} := 1 - \text{SSIM3D}$ , and  $\mathcal{L}_1$ . Additionally, in the  $k$ -space domain, we use the normalized mean absolute error (NMAE) defined as  $\mathcal{L}_{\text{NMAE}} := \text{NMAE}$ . The definitions of these components are based on prior work [34].

**Data Preprocessing** As detailed in Section 2.3, each MLP component  $\mathcal{M}_{\psi_m}$  within each cascade receives a flattened image as input, which requires a fixed input shape due to the MLP’s fixed number of features. To achieve this, all data were center zero-padded to match the largest spatial size in the dataset, i.e.,  $(n_1, n_2) = (512, 246)$ . This process involved transforming the multi-coil  $k$ -space data into the image domain using the inverse Fourier transform, applying center zero-padding, and then transforming the data back into the frequency domain via the Fourier transform.

Data were normalized using the 99.5<sup>th</sup> percentile value of the magnitude of the fully sampled autocalibration signal for each case:

$$s = \text{quantile}_{99.5}(|\mathbf{y}_{\mathcal{A}_{\text{acs}}}|). \quad (\text{B1})$$

**Sampling Schemes** In our experimental setup we consider predetermined or random schemes for comparison to our proposed methodology. Following the algorithms available in the literature [36] we specifically consider:

- Equispaced (1D/line): Lines selected at fixed intervals based on the desired acceleration, with a randomly selected offset.
- Random (1D/line): Lines selected from a uniform distribution up to the desired acceleration.
- Gaussian 1D (1D/line): Lines selected from a 1D Gaussian distribution with mean  $\mu = n_2/2$  and standard deviation  $\sigma = 4\sqrt{\mu}$ .
- Gaussian 2D (2D/point): Samples drawn from a 2D Gaussian distribution with mean  $\boldsymbol{\mu} = (n_1/2, n_2/2)$  and standard deviation  $\boldsymbol{\Sigma} = 4\mathbf{I}\sqrt{\boldsymbol{\mu}}^T$ .
- Radial (2D/point): Samples selected in a radial fashion on the Cartesian grid using the CIRCUS method.

For the above, in frame-specific experiments a distinct (arbitrary random seed) pattern from a scheme was generated per frame, whereas for unified an identical scheme was applied to all frames.

For frame-specific experiments, within each setup, a distinct random pattern was generated per frame, while unified sampling experiments used the same pattern for all frames.

We also evaluated *kt* schemes that generate dynamic sampling with temporal interleaving, avoiding repeated sampling in adjacent frames:

- *kt*-Equispaced
- *kt*-Gaussian 1D
- *kt*-Radial

During training, arbitrary patterns were generated without fixed seeds to maximize model exposure to varied data. At inference, the seed for generating patterns was fixed for each scan/patient to ensure consistency (e.g. during validation).

**Selection of Optimal Model Checkpoints** Results were obtained using the best-performing model checkpoints, selected based on validation set performance using the SSIM metric.

**Significance Testing** In our study, we used the almost stochastic order (ASO) test [5] with a significance level of  $\alpha = 0.05$  to compare reconstruction metrics between models due to its robustness in handling complex data distributions. Traditional parametric tests, such as the t-test, assume that the differences between models follow a normal distribution and have equal variances. However, these assumptions are not always valid in deep learning contexts where data distributions can be highly irregular and performance metrics can be influenced by various stochastic factors. ASO does not rely on such assumptions. Instead, it evaluates the degree to which one distribution stochastically dominates another, providing a more reliable assessment of significance when comparing models. This approach is particularly suitable for deep learning applications where performance metrics can be non-normally distributed and vary across experiments.

### B.3 Reconstruction Model Robustness Experiments

To assess the robustness of our end-to-end pipeline, we repeated the comparative studies using a state-of-the-art reconstruction model, specifically the Model-based neural network with enhanced deep learned regularizers (MEDL-Net) [20], instead of vSHARP. Below, we provide details on the optimization process and architectural design.

### B.4 Optimization

The models were developed in PyTorch [17], following the same training scheme as our main experiments. We used the Adam optimizer with an initial learning rate of  $1 \times 10^{-3}$ , which increased linearly to  $3 \times 10^{-3}$  over 2,000 iterations and subsequently decreased by 20% every 10,000 iterations, over a total of 52,000 iterations. Experiments were conducted on single NVIDIA A6000 or A100 GPUs with a batch size of 1.

For training, we adopted the loss function proposed by the authors in the original publication [20], computed exclusively in the image domain:

$$\mathcal{L} = \sum_{j=1}^T w_j \sum_{t=1}^{n_f} \mathcal{L}_{\text{MSE}}(\hat{\mathbf{x}}_t^{(j)}, \mathbf{x}_t^*), \quad w_j = \begin{cases} 0.1, & j = 1, \dots, T-1 \\ 1, & j = T \end{cases}. \quad (\text{B2})$$

where  $\{\hat{\mathbf{x}}^{(j)}\}_{j=1}^T$  denotes the predicted dynamic images from MEDL’s unrolled steps, and  $\mathcal{L}_{\text{MSE}}$  the mean squared error loss function.

### B.5 Hyperparameter Settings

For sensitivity map estimation, we used an SMP configuration identical to that in our adaptive sampling experiments. Similarly, in our adaptive sampling experiments, the ADS model module was configured identically to that in the vSHARP-based reconstruction experiments (see Section II.F.3 of the main paper). For MEDL, we employed the default hyperparameters as specified in the corresponding publication [20].

## C Quantitative Results

### C.1 Supplementary Results

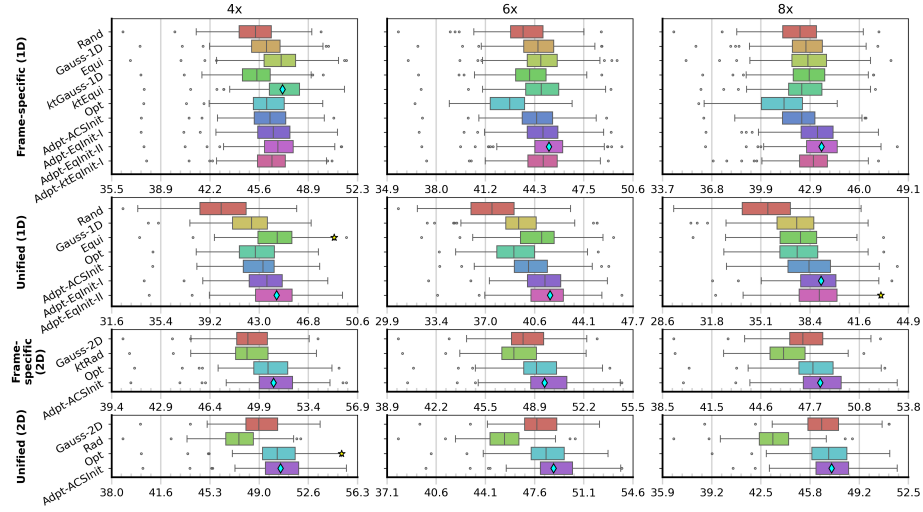


Fig. C1: PSNR metrics across all experimental settings and setups. Diamonds (◇) on the box-plot median indicate the average best methods. A star (★) on the upper whisker indicates non-significance in comparison to the average best method.

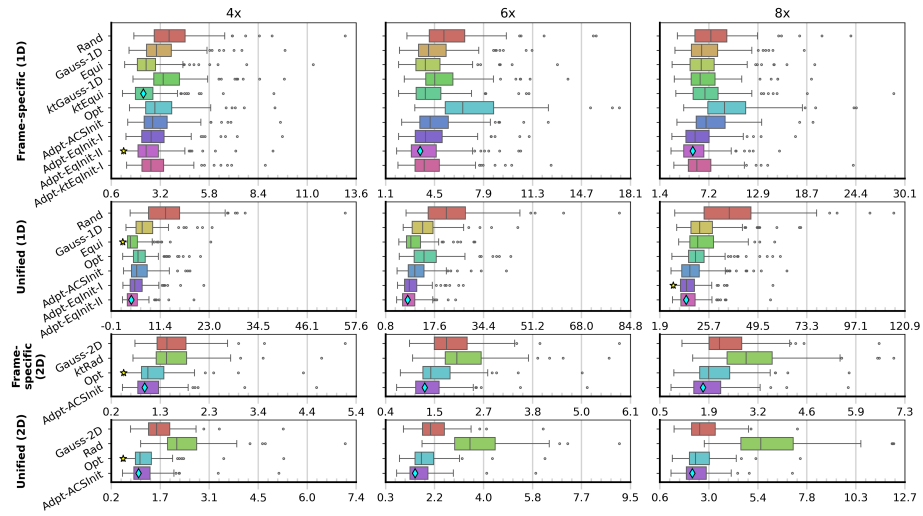


Fig. C2: NMSE ( $\times 100$ ) metrics across all experimental settings and setups. Diagonals ( $\diamond$ ) on the box-plot median indicate the average best methods. A star ( $\star$ ) on the lower whisker indicates non-significance in comparison to the average best method.



## C.2 Ablation Results

Table C1: Average results for using a single cascade ( $N = 1$ ). **Bold** numbers indicate better performance than using two cascades ( $N = 2$ ).

Method		4×			6×			8×		
		SSIM	pSNR	NMSE	SSIM	pSNR	NMSE	SSIM	pSNR	NMSE
Frame-specific (1D)	Adpt-ACSInit-N1	<b>0.9879</b>	<b>46.43</b>	<b>0.0030</b>	<b>0.9848</b>	<b>45.11</b>	<b>0.0041</b>	<b>0.9815</b>	<b>43.89</b>	<b>0.0053</b>
	Adpt-EqInit-II-N1	0.9878	46.62	0.0029	0.9841	44.97	0.0042	0.9793	43.45	0.0059
Frame-specific (2D)	Adpt-ACSInit-N1	0.9937	50.92	0.0011	0.9922	<b>49.75</b>	<b>0.0014</b>	0.9902	<b>48.54</b>	<b>0.0018</b>
Unified (1D)	Adpt-ACSInit-N1	0.9744	42.61	0.0072	0.9633	39.89	0.0134	0.9503	37.97	0.0201
	Adpt-EqInit-II-N1	0.9753	42.85	0.0070	0.9628	40.31	0.0124	0.9452	37.92	0.0212
Unified (2D)	Adpt-ACSInit-N1	0.9930	50.45	0.0012	0.9910	48.99	0.0017	0.9880	47.33	0.0024

Table C2: Average results for allowing the adaptive sampler to non uniformly allocate the sampling budget across time-frames.

Method		4×			6×			8×		
		SSIM	pSNR	NMSE	SSIM	pSNR	NMSE	SSIM	pSNR	NMSE
Frame-specific	Adpt-NU	0.9881	46.32	0.0031	0.9833	44.34	0.0048	0.9755	41.91	0.0085
(1D)	Adpt-NU-N1	0.9873	46.27	0.0031	0.9830	44.58	0.0047	0.9769	42.46	0.0075

### C.3 Reconstruction Model Robustness Results

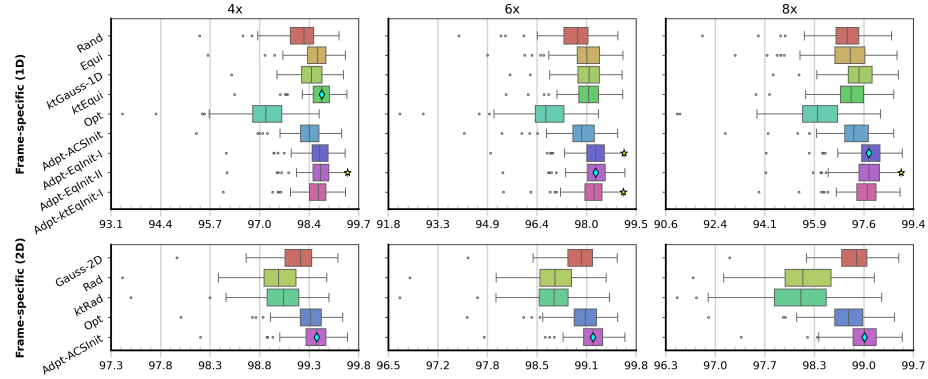


Fig. C3: SSIM ( $\times 100$ ) metrics across all experimental settings and setups using MEDL as a reconstruction network. Diamonds ( $\diamond$ ) on the box-plot median indicate the average best methods. A star ( $\star$ ) on the lower whisker indicates non-significance in comparison to the average best method.

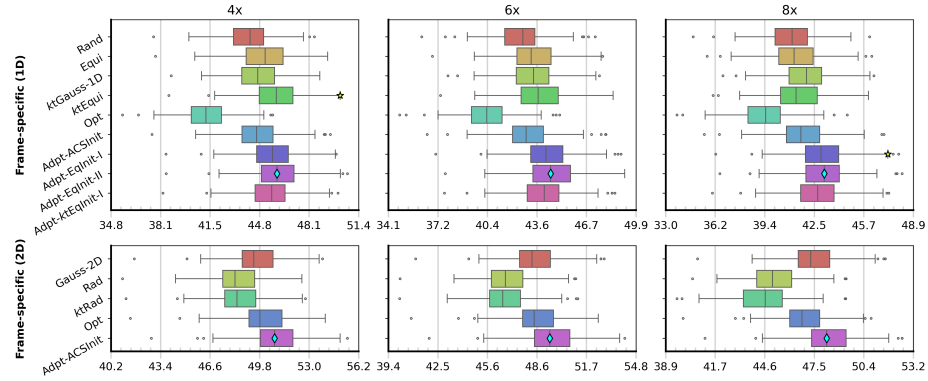


Fig. C4: PSNR metrics across all experimental settings and setups using MEDL as a reconstruction network. Diamonds ( $\diamond$ ) on the box-plot median indicate the average best methods. A star ( $\star$ ) on the lower whisker indicates non-significance in comparison to the average best method.

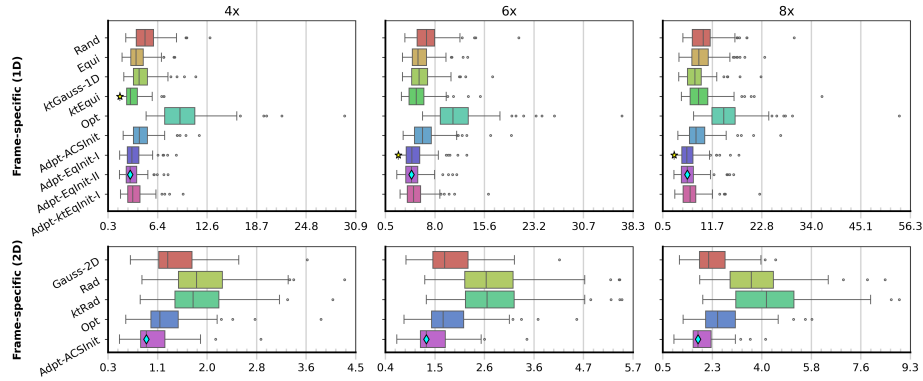


Fig. C5: NMSE ( $\times 100$ ) metrics across all experimental settings and setups using MEDL as a reconstruction network. Diamonds ( $\diamond$ ) on the box-plot median indicate the average best methods. A star ( $\star$ ) on the lower whisker indicates non-significance in comparison to the average best method.

## D Qualitative Results

In this section we illustrate examples of produced subsampling patterns and reconstructions across all experiments (phase-specific or unified, 1D or 2D sampling) and setups (fixed or learned). Black lines or points indicate fixed or initial pattern (applicable only to learned if initial), and red lines or points indicate learned pattern. Cyan boxes mark the SSIM values.

### D.1 Phase-Specific Experiments

#### Subsampling Patterns

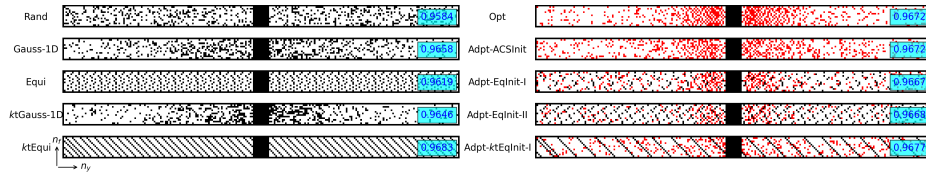


Fig. D1: Example of patterns from the test set across setups for frame-specific sampling at  $R = 4$ .

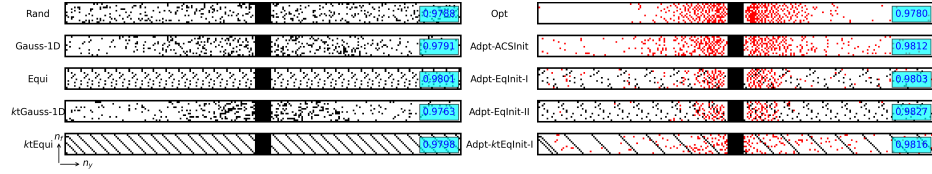


Fig. D2: Example of patterns from the test set across setups for frame-specific sampling at  $R = 6$ .

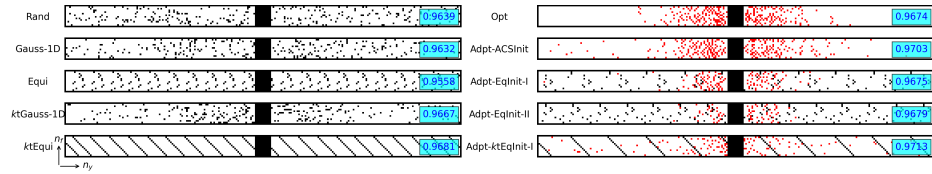


Fig. D3: Example of patterns from the test set across setups for frame-specific sampling at  $R = 8$ .

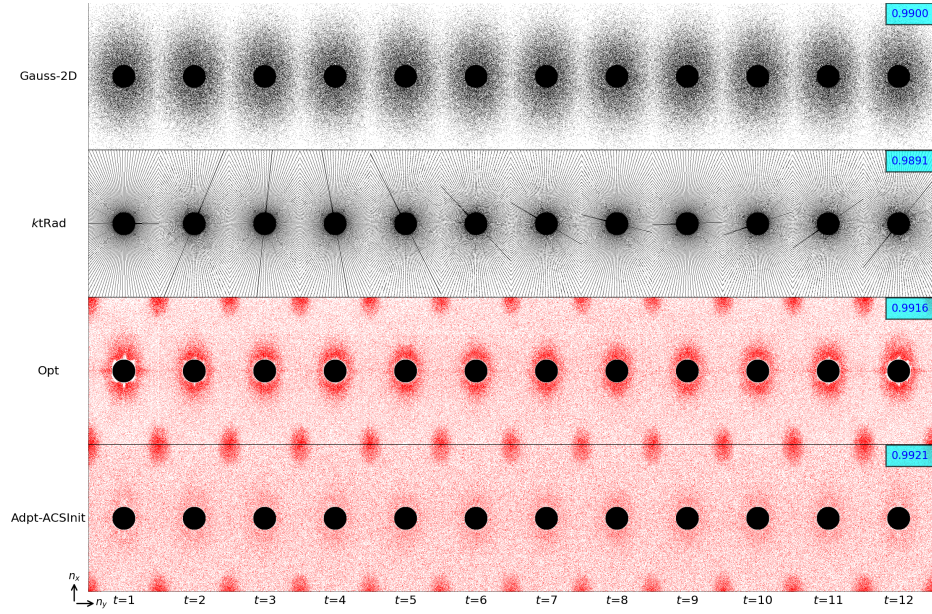


Fig. D4: Example of patterns from the test set across setups for frame-specific 2D sampling at  $R = 4$ .

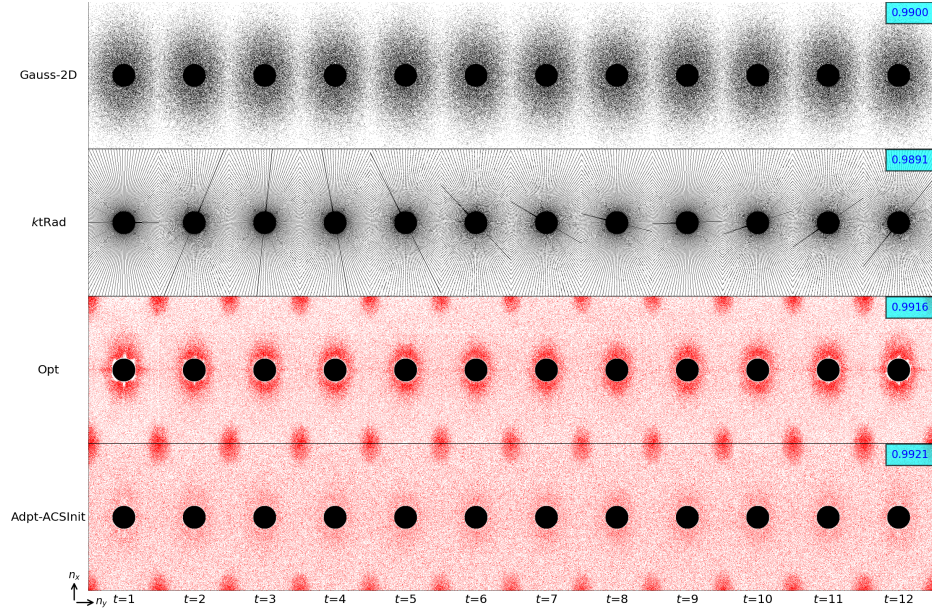


Fig. D5: Example of patterns from the test set across setups for frame-specific 2D sampling at  $R = 6$ .

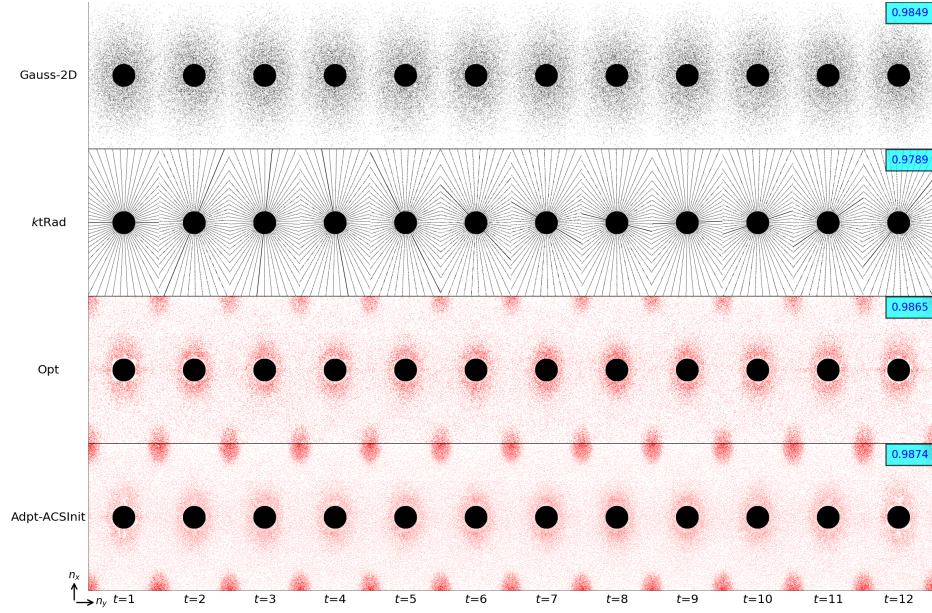


Fig. D6: Example of patterns from the test set across setups for frame-specific 2D sampling at  $R = 8$ .



## Reconstructions

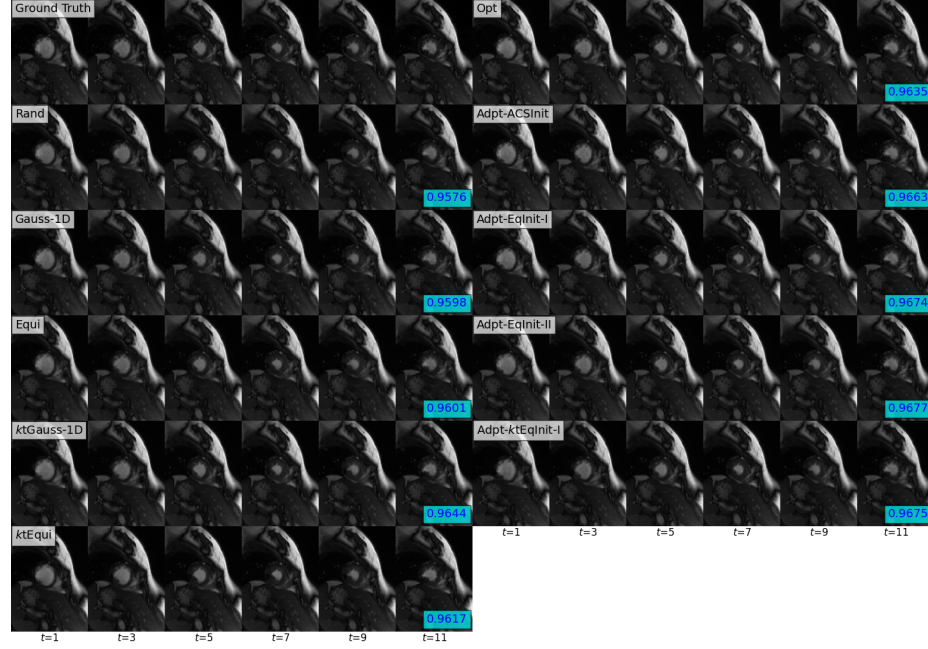


Fig. D7: Example of reconstructions from the test set across setups for frame-specific 1D sampling at  $R = 8$ .

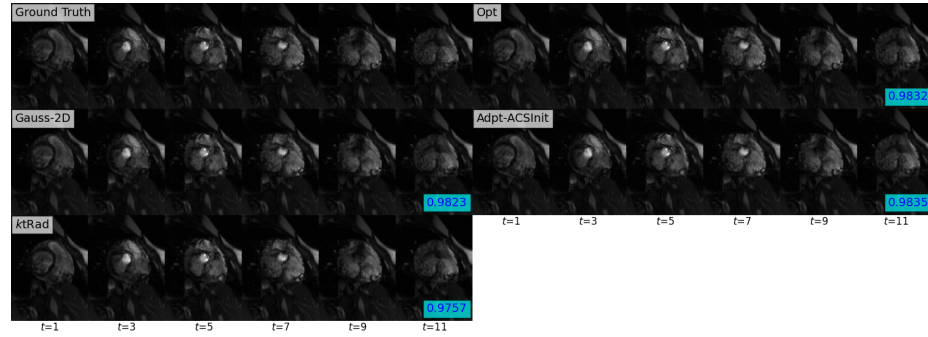


Fig. D8: Example of reconstructions from the test set across setups for frame-specific 2D sampling at  $R = 8$ .

## D.2 Unified Experiments

### Subsampling Patterns

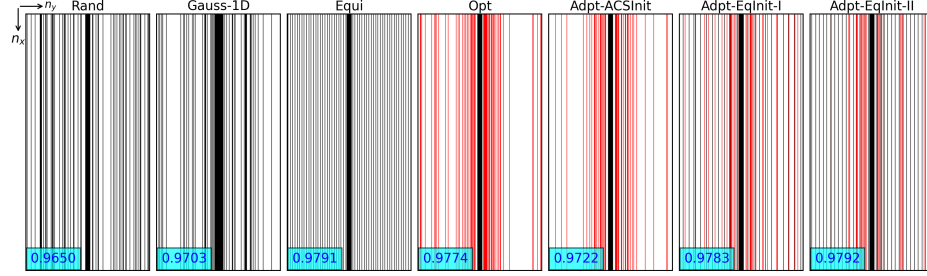


Fig. D9: Example of patterns from the test set across setups for unified sampling at  $R = 4$ .

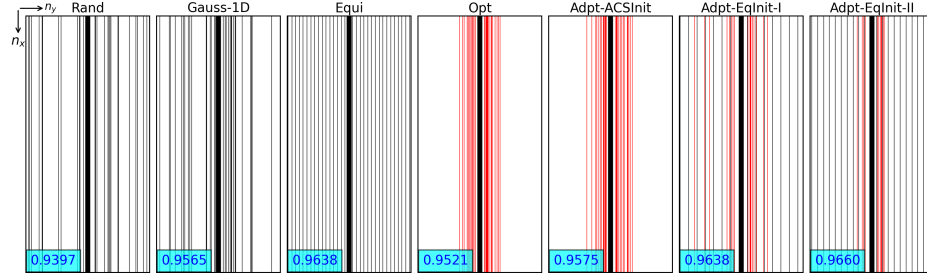


Fig. D10: Example of patterns from the test set across setups for unified sampling at  $R = 6$ .

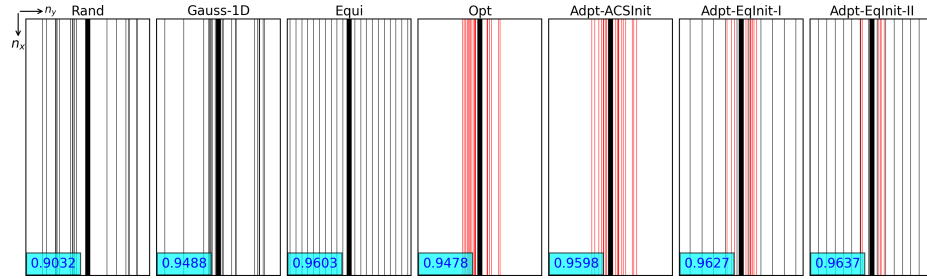


Fig. D11: Example of patterns from the test set across setups for unified sampling at  $R = 8$ .

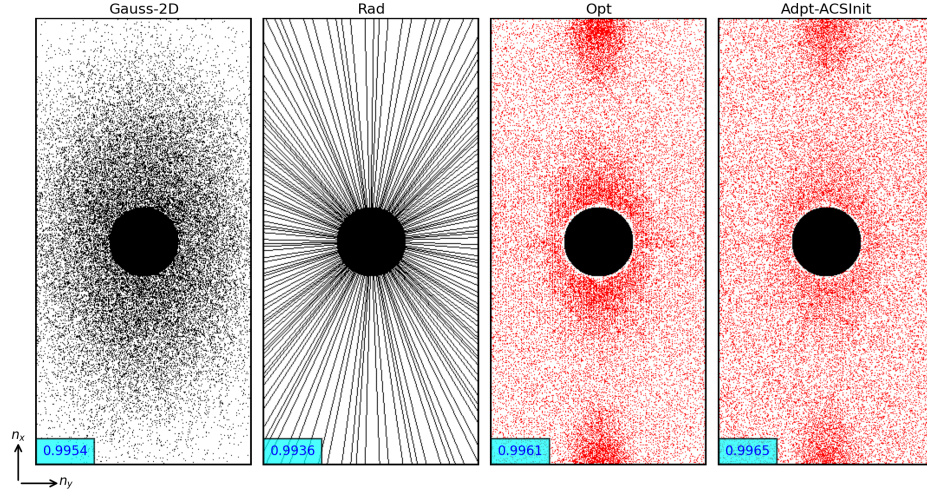


Fig.D12: Example of patterns from the test set across setups for unified 2D sampling at  $R = 4$ .

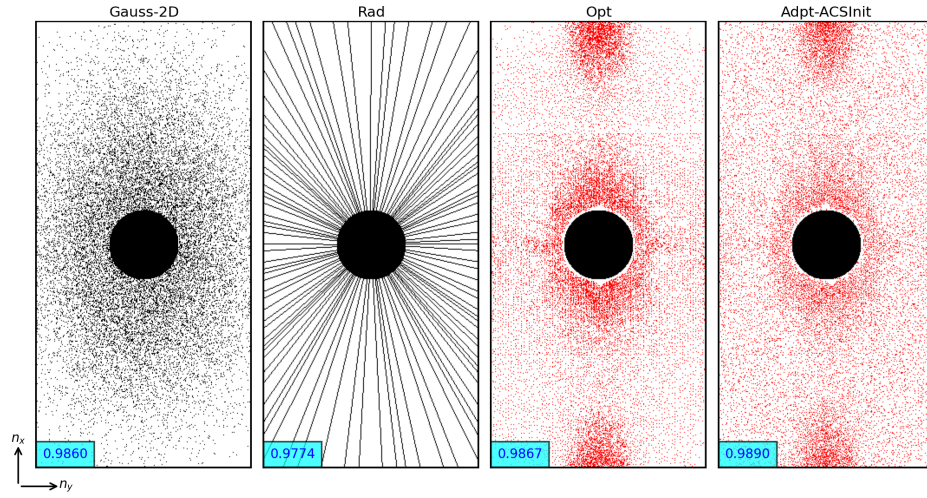


Fig.D13: Example of patterns from the test set across setups for unified 2D sampling at  $R = 4$ .



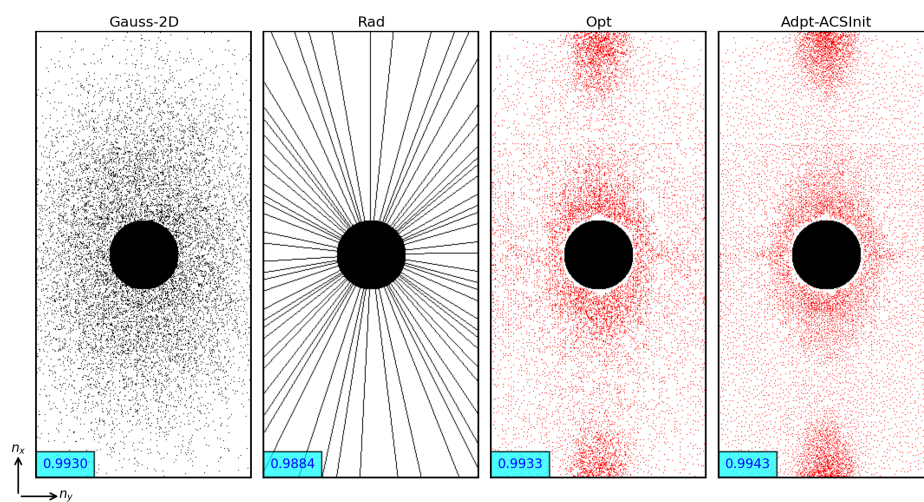


Fig. D14: Example of patterns from the test set across setups for unified 2D sampling at  $R = 8$ .

## Reconstructions

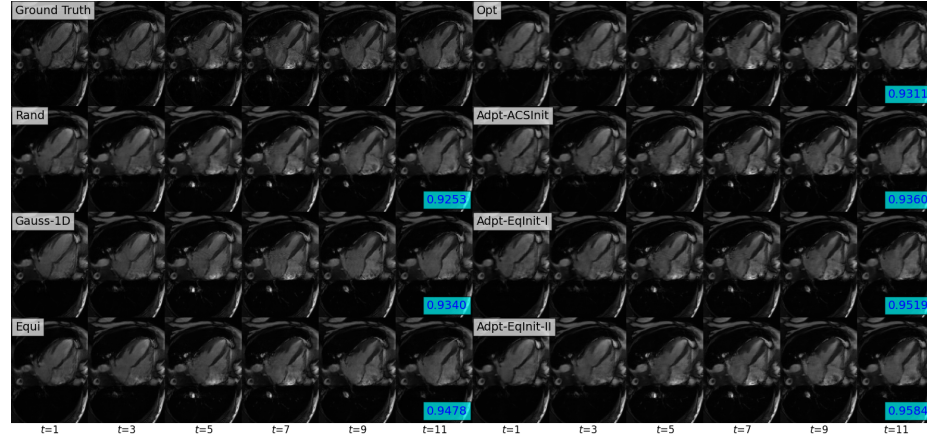


Fig. D15: Example of reconstructions from the test set across setups for unified 1D sampling at  $R = 8$ .

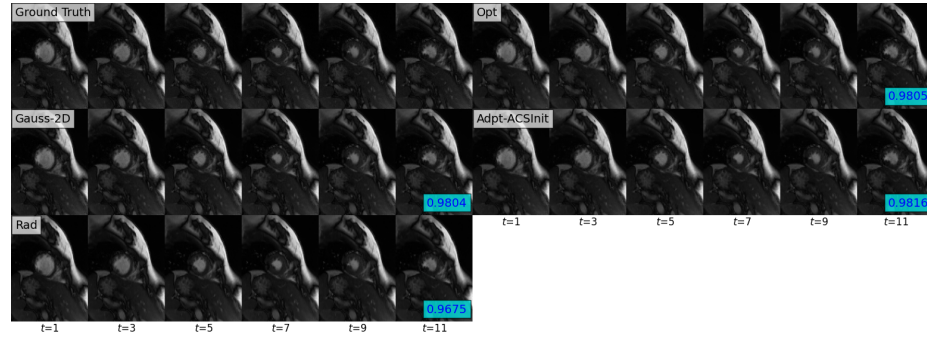


Fig. D16: Example of reconstructions from the test set across setups for unified 2D sampling at  $R = 8$ .